

Main Manuscript for

Graphics Processing Unit Assisted Computation for a Gas-Phase Chemical Solver in a Regulatory Chemical Transport Model

Khanh Do^{1,2}, George Delic³, José Rodríguez Borbón⁴, Duncan Quevedo⁵, Bryan M. Wong⁴, and Cesunica Ivey^{2,5,*}

¹Department of Chemical and Environmental Engineering, University of California, Riverside, CA, 92521

²Center for Environmental Research and Technology, Riverside, CA, 92507

³Hiperism Consulting, LLC, Chapel Hill, NC, 27514

⁴Materials Science and Engineering Program, University of California, Riverside, CA, 92521

⁵Department of Civil and Environmental Engineering, University of California, Berkeley, CA, 94720

*Cesunica E. Ivey, corresponding author

Email: iveyc@berkeley.edu

Author Contributions: K.D., B.M.W., and C.I. designed the research; K.D. and J.R.B. performed the research; K.D. analyzed the data; K.D., G.D., and C.I. wrote the paper; J.R.B., D.Q. and B.M.W. edited the paper.

Competing Interest Statement: The authors declare no competing interests.

Keywords: graphics processing unit; air quality model; chemical solver

This PDF file includes:

Main Text
Figures 1 to 9

This manuscript is a non-peer reviewed preprint submitted to EarthArXiv and is currently undergoing peer review.

Abstract

The Earth's atmosphere is extremely complex due to the presence of several dynamic processes, such as dispersion, diffusion, deposition, and chemical reactions. There is a pressing need to improve the predictability of air quality models by integrating more of these scientific processes with an increasing number of chemical species into the mechanisms. These enhancements degrade the computational efficiency of the most comprehensive modeling applications, leading to a significant increase in simulation time. Offline chemical transport models (CTM) spend considerable time simulating large atmospheric domains, primarily on solving for the gas-phase chemistry. To reduce the simulation time while maintaining the integrity of the models, we utilized graphics processing units (GPUs) to replace the central processing units (CPU) for computing the most expensive science processes by successfully migrating the gas-phase chemistry solver onto a GPU to reduce computational time. The actual kernel computing time for the solver is twice as fast as the CPU with the BLKSIZE of 8,000; however, the GPU solver incurs communication time costs due to the of moving data back and forth between the CPU host system memory to the GPU memory. In this paper, we focus on compiling of the Community Multiscale Air Quality (CMAQ) model with CUDA kernels, migrating the gas-phase CTM solver onto the GPU, and optimizing the solver to improve GPU computational efficiency. Our positive results from the migrated solver show significant promise for intensive parallel computing applications on GPU devices reduce simulation time and accelerating air quality research.

MAIN

Introduction

Deterministic air quality models (AQMs) are designed to simulate complex physical and chemical processes in the Earth's atmosphere with mathematical representations of atmospheric transport, diffusion, dispersion, and chemical reactions. The governing equations are solved by analytical and numerical techniques and are based on the conservation of mass (which is not conserved in CMAQ) for air pollutants of interest (1, 2). The use of full-scale, deterministic AQMs requires a diversity of input data, including meteorology (e.g., wind, temperature, and relative humidity), emissions of primary air pollutants, topography, and land cover. In the United States, AQMs are often utilized to support compliance with the U.S. National Ambient Air Quality Standards for six criteria air pollutants: fine and coarse particulate matter (PM), ozone (O₃), carbon monoxide (CO), sulfur dioxide (SO₂), nitrogen dioxide (NO₂), and lead (Pb) (3, 4).

Recently, with the rapid growth of machine learning (ML) accessibility, empirical AQMs have become more useful for research purposes by speeding up analyses, and modeled outcomes rely fully on empirical relationships between historical data (5). However, ML models have not been standardized for regulatory decision-making, and conclusions drawn from ML applications are best grounded with the first principles relationships that govern deterministic AQMs. As utilizing ML algorithms for environmental predictions has become more prevalent for improving research efficiency, advancements in computational hardware are also promising for improving efficiency. This study explores the latter for improving efficiency within a regulatory AQM that is commonly used for NAAQS attainment demonstrations and evaluation of emission control strategies.

The CMAQ Model

The Community Multiscale Air Quality (CMAQ) is a chemical transport AQM (CTM) developed within the U.S. Environmental Protection Agency and is commonly used to develop emissions control strategies for criteria air pollutants (6–8) and quantify the impact of distinct air pollution sources (9, 10). The model is one of the most widely used in air quality modeling systems in recent years (11). Generally, advancements in chemical mechanisms and transport have improved the

accuracy of AQMs and the ability to reproduce atmospheric air pollution concentrations at monitored locations (12–16).

The CMAQ model has two popular chemical mechanisms: Carbon Bond (CB) (17) and the Statewide Air Pollution Research Center (SAPRC) (18) mechanisms. SAPRC was developed to improve the characterization of atmospheric reactions of volatile organic compounds (VOCs) in the presence of NO_x as well as the formation O₃ and other secondary air pollutants (19). Updated versions of the SAPRC mechanism in later years give better predictions for secondary pollutants by adding a significant number of species. The number of model species for SAPRC99, SAPRC07, and SAPRC18 are 82, 126, and 516, respectively. Correspondingly, with the increase in mechanism species, chemical reactions also increase, with 211 reactions for SAPRC99, 569 reactions for SAPRC07, and 1772 reactions for SAPRC18 (20). CMAQ is precise in representing atmospheric physics and chemical processes, but not surprisingly, the simulation time is proportional to the number of chemical reactions.

Parallel Computation with CPUs

Current AQMs are designed to utilize central processing units (CPUs) to carry out the abovementioned chemical and physical processes. With a set of instructions, scheduler, and high clock speed, CPUs are superior for arithmetic operations, and programming languages optimize compiled code to execute on commodity CPU architectures. The 3-dimensional space of CMAQ's grid is subdivided into 3-dimensional grid cells, and the spatial resolution of the simulation domain is defined by user inputs. CMAQ uses the Message Passing Interface (MPI), a message-passing standard, to execute the simulation process in parallel mode, where multiple grid blocks simultaneously execute on any number of available CPU cores. Data in multiple grid blocks must be explicitly shared by passing messages between MPI processes (21–23). Whenever synchronization between MPI processes is required at MPI barrier calls (as is the case of CMAQ), this comes at the cost of simulation time.

CPUs are fast for arithmetic operations, and CMAQ simulation time decreases as the number of CPU cores increases because each MPI process utilizes a separate CPU core. Thus, the MPI scaling is limited by the core count per CPU. For current consumer CPUs, the core count ranges from up to 48 for Intel CPUs and up to 16 for AMD CPUs. One of the best CPU models for server platforms is the AMD EPYC 7773X with 64 cores but comes at a premium cost of \$8,800 (as of April 2023). To accelerate the simulation, researchers may purchase expensive high-performance computing (HPC) clusters or pay a premium for cloud services, such as Microsoft Azure or Amazon Web Services.

Computational Challenges

Governing equations within full-scale CTMs are solved using the arithmetic logical units (i.e., building blocks) of CPUs within HPC systems. In regard to runtime, for example, a 12 km horizontally spaced, two-way coupled WRF-CMAQ simulation with 34 layers of variable thickness and a domain size of 279 x 251 grid cells requires over three hours of wall clock time for one simulated day when utilizing 32 CPU cores (24). In a preceding study, we simulated five months (1 May – 30 Sep 2017) of ozone concentrations for Southern California using 4 km horizontal spacing and a domain size of 156 x 102 grid cells, and the wall clock time was 10 days when utilizing 16 MPI processes (i.e., ~1.6 hours per simulated day with 8 CPU cores) (5).

The computational efficiency of CMAQ is largely inhibited by the need to solve a set of sparse, stiff, first-order differential equations when computing the gas-phase chemical concentrations (25). For a cursory overview, see Chapter 16 of Press et al. (1992) (26). Moreover, for the SAPRC07 implementation in CMAQ, the system of gas-phase reactions is calculated using one of three numerical solvers: Euler Backward Iteration (EBI) (26), Rosenbrock (ROS3) (26), or sparse-matrix vectorized Gear (SMVGEAR) (27, 28). The selected solver is invoked for every time step and grid cell (row x column x height) for all species in the SAPRC07 mechanism until a specified convergence tolerance is met. The wall clock time is linearly proportional to the grid size of the simulated domain and exponentially proportional to the number of chemical species.

GPU architecture and performance

Graphics processing units were traditionally developed to accelerate graphic rendering for output to display devices. In graphics rendering, a single set of instructions is executed on multiple GPU cores, emphasizing parallel processing of one specific task. Modern GPUs are capable of computing vector operations with floating-point arithmetic. New-generation GPUs can handle double-precision floating point numbers to improve model accuracy (29, 30). In 2006, NVIDIA launched Compute Unified Device Architecture (CUDA), the first commercial solution for general-purpose computing on GPUs (GPGPU). CUDA has provided unique frameworks that allow developers to integrate GPU computing across different programming languages. CUDA has also become an effective tool for training deep learning and machine learning models.

Despite low clock speed and a naïve scheduler, GPUs still outperform CPUs for multithread applications (31). Ada Lovelace architecture GPUs from NVIDIA have up to 16,384 CUDA cores with a 2.52 GHz boost clock and 24 GB of GPU memory (NVIDIA RTX 4090). Many CUDA cores enable a GPU to perform thousands of arithmetic operations simultaneously, significantly benefiting from parallelized computing and extensive data handling. In parallel computation, multiple GPU streams perform simple operations, and all processes in all GPU threads are identical. Therefore, GPU computing is frequently more affordable and scalable than CPU-based HPCs with several nodes. In comparison to a CPU-based system, the cost of an NVIDIA RTX 4090 is \$1,599 (as of April 2023). Further, GPUs can be installed into an existing personal computer, thereby increasing its computational efficiency without the need for dependence on less accessible HPC systems.

GPU application for CMAQ

With the popularity of GPGPU and the improvement of CUDA from NVIDIA, air quality researchers have sought alternative solutions to accelerate CTMs. Delic has shown that migrating a selected loop of CMAQ to a GPU was feasible (32). More recently, Cao et al. successfully migrated the horizontal advection process (HAVDPPM) from CAMx onto a GPU (33). The gain for GPU-HAVDPPM was substantial compared to the original HAVDPPM on the CPU. However, the migration of HAVDPPM to the GPU was incomplete and not native to the Fortran programming

language. They translated HAVDPPM to C programming language before using CUDA C to execute the process on the GPU. This method reduced the overall efficiency of the computation due to the heterogeneity in Fortran and C programming languages.

Our work introduces the implementation of CMAQ chemical solvers for the SAPRC07 gas-phase mechanism onto GPUs using NVIDIA's CUDA programming platform, which is based on Fortran, the native programming language of the CMAQ model. We sought to improve the overall CMAQ simulation time by migrating this intensive computational process onto GPUs. Specifically, we migrated the partial derivative, sparse LU decomposition, and back substitution subroutines of the ROS3 (Rosenbrock) solver to the CUDA platform. Our CPU-GPU version of the CMAQ model was tested for a 4 km simulation over Southern California with a domain size of 102 x 156 x 11 grid cells. In exploring the GPU architecture, the advantages and the disadvantages of GPU programming were also investigated.

Results

Timing of science process

The science process modules in CMAQ have different computational times and hardware resource requirements that are non-uniform across the modules. We timed five processes for one simulation day on a host CPU to benchmark the model's computational performance in the native configuration (Figure 1). The gas phase chemistry was the most time-consuming step, taking five times longer than the vertical diffusion and horizontal advection processes and significantly impacting the overall CMAQ simulation duration when using fewer CPU cores. Therefore, we focus on the migration of the gas-phase chemistry module onto the GPU to improve overall computational performance.

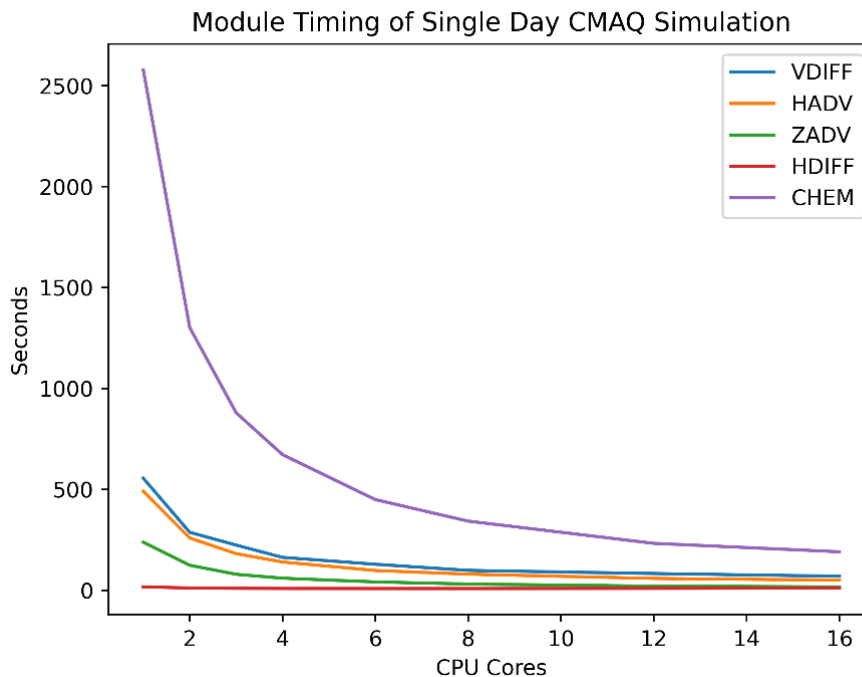


Figure 1. Module timing of a single simulated day for five science modules in CMAQ. Gas-phase chemistry (CHEM, purple) is the slowest module across all CPU cores. Legend entries are vertical diffusion (VDIFF), horizontal advection (HADV), vertical advection (ZADV), horizontal diffusion (HDIFF), cloud processes (CLDPROC), and gas-phase chemistry (CHEM).

Effects of BLKSIZE parameter

The BLKSIZE parameter in CMAQ can be modified before compiling CMAQ for the SMVGEAR and ROS3 solvers, and the consequences for performance are critical because of cache alignment issues. The default BLKSIZE is 50, and BLKSIZE influences the way CMAQ distributes the grid cells for parallel computation. A large BLKSIZE results in fewer function calls for a given domain, and the solver effectively uses large matrices, supporting the utility of GPU computing for this application. The spatial dimensions of the CMAQ grid are 102 x 156 x 11 (row x column x layer) cells, resulting in 175,032 total grid cells. Therefore, if the BLKSIZE is 50, CMAQ calls the gas-chem solver ~3,500 times. When the BLKSIZE is set to 2,000, the gas-chem solver is called 88 times. However, the concentration matrix is 40 times larger than the BLKSIZE choice of 50.

The CHEM science module and other science process modules were timed for one iteration timestep (Figure 2). The simulation time of the science processes increased solely due to the computation time of the gas-phase chemistry, and other science processes' computing time, such as diffusion, advection, or aerosol, is unaffected by the BLKSIZE (other process descriptions in *SI Appendix, section S1*). Larger BLKSIZE choices degraded CMAQ performance; with BLKSIZE of 10,000, CMAQ is about 3.5 times slower than the default BLKSIZE. Increasing the BLKSIZE did not influence CMAQ simulation time towards ideal conditions. However, because of the limitations of hardware, big concentration matrices due to large BLKSIZE cause an overflow of the CPU cache (34–36). When the CPU performs matrix operations, the CPU has to retrieve the data from the system memory through several cache layers and this causes the CPU to stall if the memory address is not found in the table lookaside buffer. Therefore increasing the BLKSIZE above a certain range has a negative effect on the overall CMAQ simulation time.

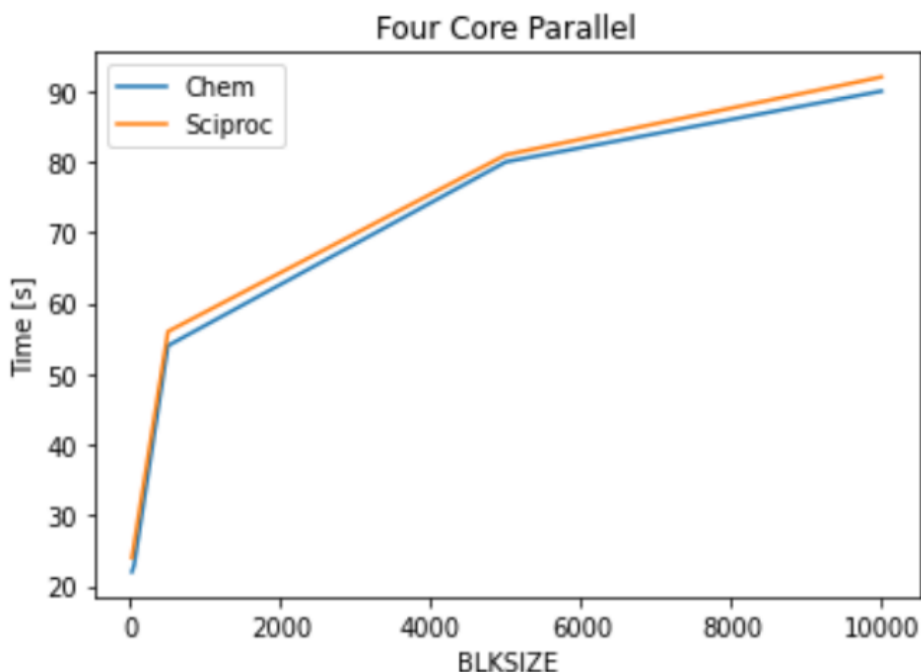


Figure 2. Effect of BLKSIZE on CMAQ's science processes per simulation timestep. The blue line is the gas-phase chemistry process (Chem), and the orange line represents all science processes (Sciproc).

Initial GPU Performance: CMAQ-CUDA v1.0

Initial GPU implementation of the CHEM process was designed for the GEAR solver, and subroutines were timed to assess the computational performance of the new configuration, CMAQ-CUDA v1.0 (Figure 3). The slowest subroutines are the calculation of the partial derivative (PDERIVE, 0.2 ms) and matrix decomposition (DECOMP, 0.3 ms). PDERIVE computes a partial derivative of the concentration matrix with respect to the chemical species, and DECOMP performs LU decomposition of the partial derivative matrix into the form of lower and upper triangular matrices. This version of the GPU migration of the solver prioritizes the slower subroutines to optimize the configuration's performance.

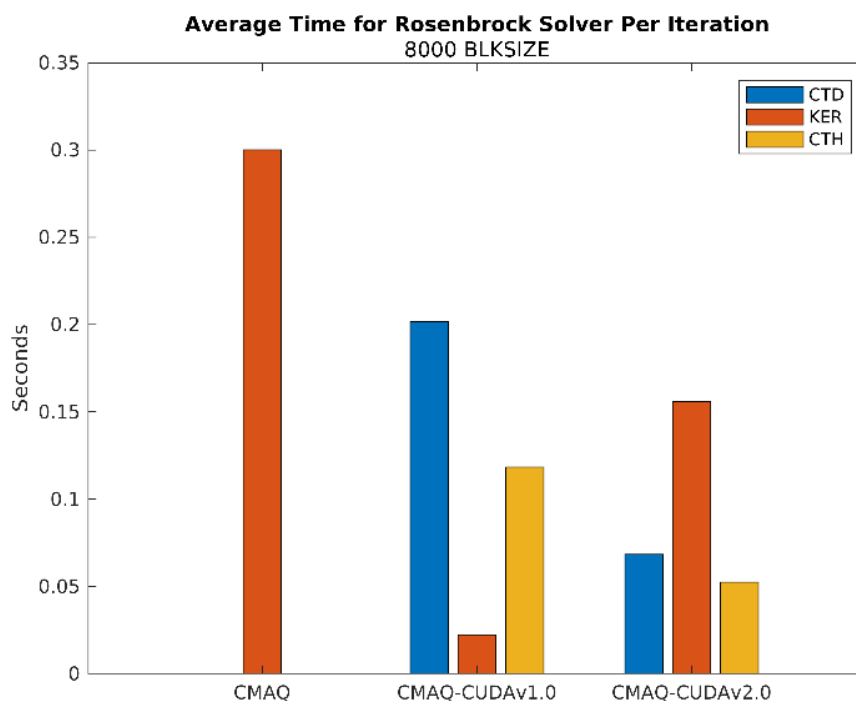


Figure 3. Average time for Rosenbrock solver for one iteration for CMAQ, CMAQ-CUDA v1.0, and CMAQ-CUDA v2.0. Blue bars are the time to copy data to the GPU device (CTD), orange bars are the actual computing time (KER), and yellow bars are the time for copying data from the GPU device to the CPU host (CTH).

We moved on to the Rosenbrock GPU implementation because its subroutines are better candidates for vectorization compared to GEAR subroutines. SI Appendix Section S2 provides a block diagram of the CMAQ-CUDA v1.0 implementation of the Rosenbrock solver. Subroutines with the .F extension are executed using the CPU, and the CUDA kernels with .cuf extensions are executed using the GPU. Ideally, more migrated GPU subroutines significantly improve the computational time. However, only selected subroutines can be parallelized due to data dependence. Table S1 summarizes the computing time for the four Rosenbrock subroutines performed on conventional CMAQ and CMAQ-CUDA v1.0 for BLKSIZE choices of 2,100 and 10,000. The actual GPU computing time (.cuf kernel time) is much faster than CPU time with the same number of arithmetic operations. With a BLKSIZE of 10,000, GPU computing is about 91% faster for the RBFEVAL subroutine, 86% faster for the RBJACOB subroutine, 93% faster for RBDECOMP, and 92% faster for RBSOLVE. Although the computation carried out on the GPU outperformed CPU performance, the overall CMAQ simulation time suffered from the cost of data transfer between the CPU host and the GPU device. The CMAQ-CUDA v1.0 model implemented a naïve version of the Rosenbrock solver on the GPU, in which every subroutine on the solver has its own kernel and requires multiple data transfers through a PCIe connection. When the dimensions of the concentration matrices grow larger with large BLKSIZE, GPU computing experiences performance losses due to the bandwidth bottleneck of the PCIe interface to the GPU.

Data Transfer Optimization: CMAQ-GPUv2.0

CMAQ-GPUv2.0 was developed to minimize data transfer dependencies and optimize parallel computing for the Rosenbrock solver. In this second version, we vectorized and combined the four subroutines of the solver into one .cuf subroutine to enhance the data transfer rate. The initial .F subroutine prepares all required data used by the solver and then sends the data to the GPU memory. After the .cuf kernel calculation, the RBSOLVE subroutine returns the results to the host, as shown in Figure S4. CMAQ-GPUv2.0 still requires sending the results from the GPU back to the host for the convergence test criterion. However, this configuration requires only one data transfer between the host and the device for each invocation of the Rosenbrock solver.

Figure 3 shows the average time of the Rosenbrock solver for one iteration for CMAQ, CMAQ-CUDA v1.0, and CMAQ-CUDA v2.0 for a BLKSIZE choice of 8,000. The actual computation time (orange bar) is faster with CMAQ-CUDA than with traditional CMAQ. The gain from the kernel for CMAQ-CUDA v1.0 was offset by the transfer time to the GPU device (blue bars) and the CPU host (yellow bars). The implementation of CMAQ-CUDA v2.0 optimized the transfer time and showed a significant improvement. However, the kernel of CMAQ-CUDA v2.0 experienced longer computation times due to extended arithmetic operations added to the kernel. Because more code from the RBSOLVER was migrated to the kernel of CMAQ-CUDA v2.0, the kernel had to compute a large number of serial operations, resulting in slower GPU clock speeds that degraded the overall computation time. The CMAQ-CUDA v2.0 version allocated a large amount of data on the kernel, causing the GPU memory management to be less efficient and adding extra time to search through the memory to acquire the data (37, 38). The CMAQ-CUDA v2.0 version also performed better with a large BLKSIZE. The total time for one iteration of the Rosenbrock solver, including data transfer and computation time, is shown in Figure 4. Traditional CMAQ gave a good performance with a smaller BLKSIZE, but when the BLKSIZE was greater than 3700, CMAQ-CUDA v2.0 showed better computation times.

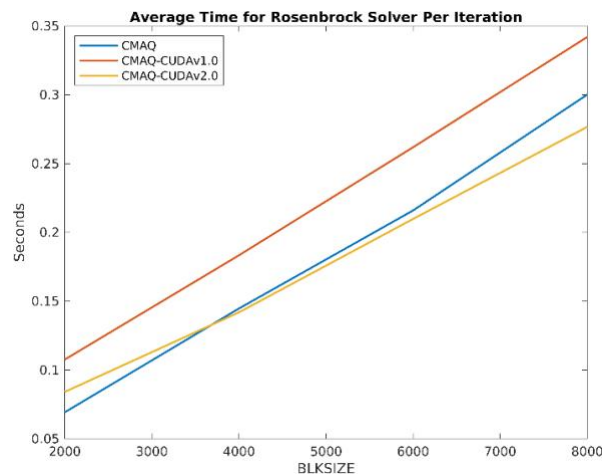
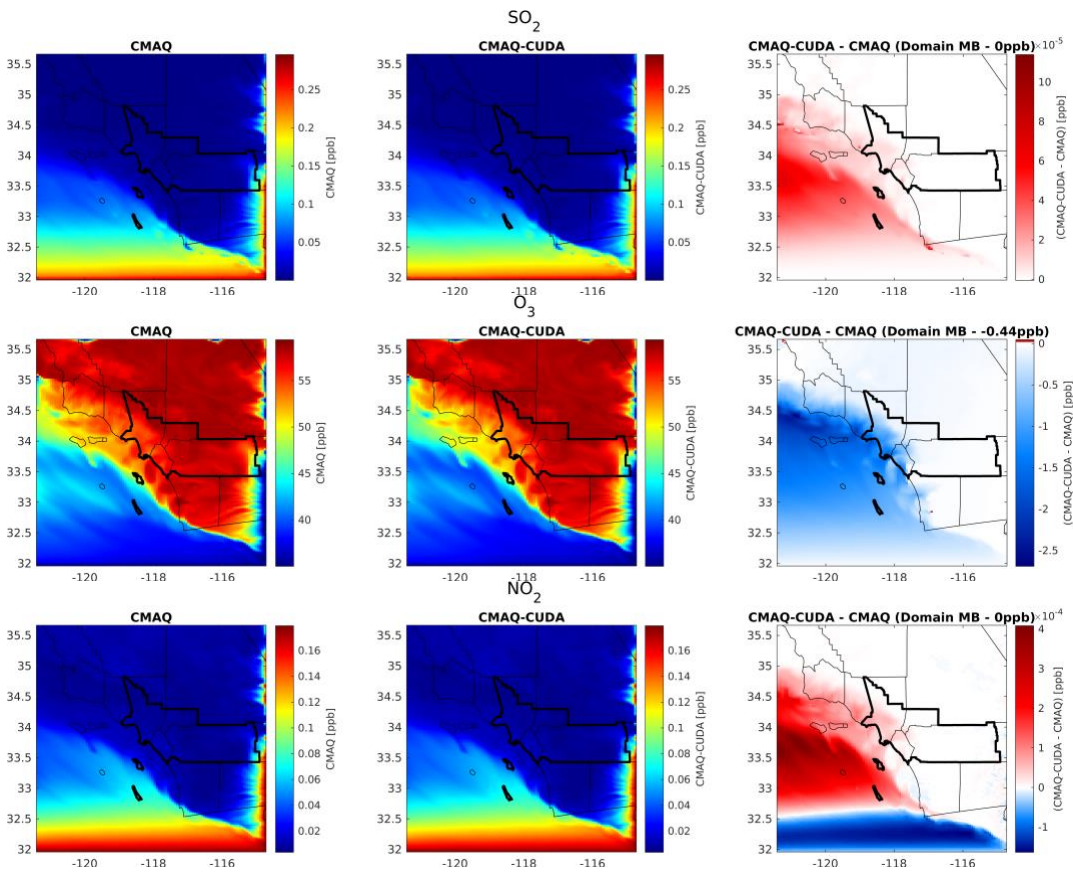
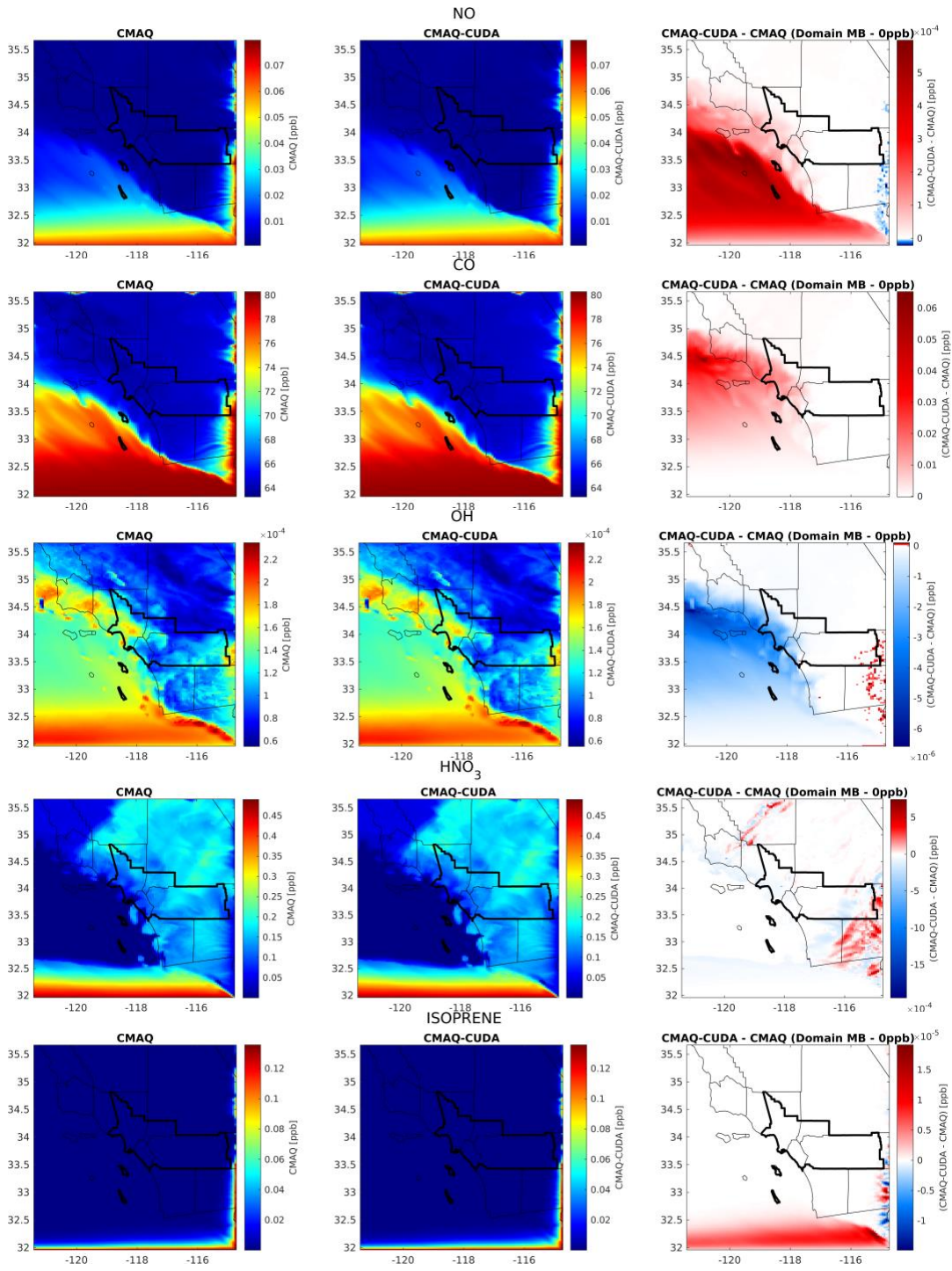


Figure 4. Average time for Rosenbrock solver for one iteration with different BLKSIZEs. The blue line is conventional CMAQ, the orange line is CMAQ-CUDA v1.0, and the yellow line is CMAQ-CUDA v2.0.

CMAQ-CUDAv2.0 Accuracy

We evaluated the accuracy of CMAQ-CUDAv2.0 by completing a 72-hour simulation and comparing the outputs with the original CMAQ CPU version. Figure 5 shows the spatial distribution of simulated concentrations of the common gaseous species: SO₂, O₃, NO₂, NO, CO, OH, nitric acid (HNO₃), isoprene, hydrogen peroxide (H₂O₂), and peroxyacetyl nitrate (PAN). The two CMAQ versions produced very similar concentrations across all the species, including the maximum and minimum values of the entire simulated domain. The mean bias over the domain is small, and the maximum errors between the two values are about 0% for SO₂ and CO, 5% for O₃, and 0.8% for NO, which are important species for NAAQS attainment demonstration.





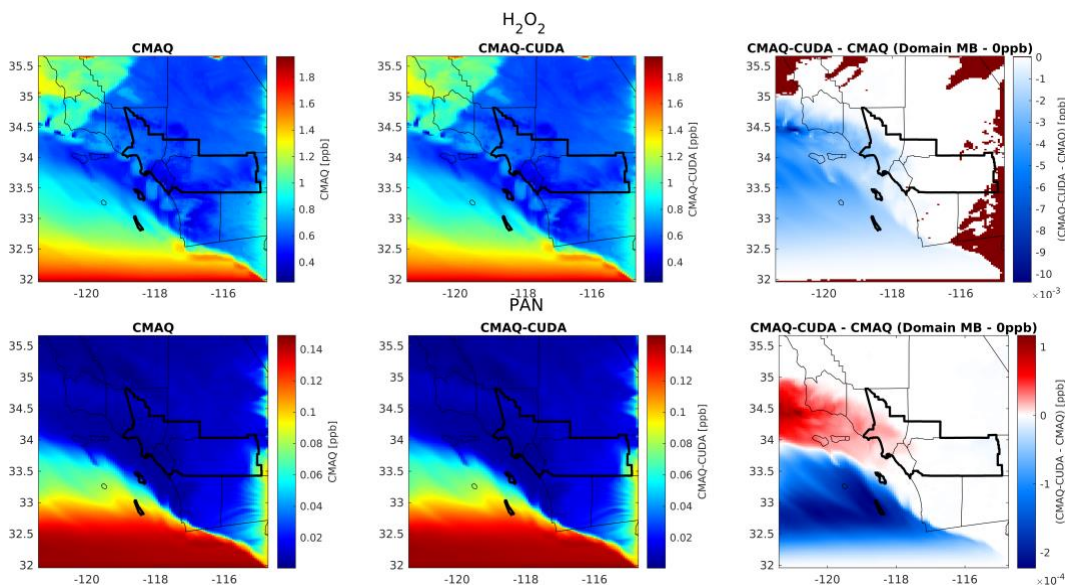


Figure 5. Outputs after 72 hours of simulation of CMAQ and CMAQ-CUDA v2.0. Results are presented for SO_2 , O_3 , NO_2 , NO , CO , OH , HNO_3 , isoprene, H_2O_2 , and PAN. The left panels are the CMAQ simulation, the middle panels are the CMAQ-CUDA v2.0 simulation, and the right panels are the differences between CMAQ and CMAQ-CUDA in ppb.

Figure S6 highlights the normalized mean bias (NMB) for SO_2 , O_3 , NO_2 , NO , CO , OH , HNO_3 , isoprene, H_2O_2 , and PAN across the entire simulation domain from May 11th to May 16th, 2017. The initialization period of the simulation for the CMAQ-CUDA largely deviated from the native CMAQ version, exhibiting notable domain-averaged biases across all output species. The minimum daily biases are observed at the middle of each simulation day. Given the spatial variability of biases across the domain (land and ocean differences), it is useful to also examine biases at regulatory air monitoring sites. Figure 6 highlights the NMB of O_3 concentrations at 27 specific locations in the South Coast Air Basin. At all sites, the maximum NMB errors occur within the first simulation day. By the fifth day, NMB dwindles to below 3%. Importantly, this trend remains consistent across all species. The NMB errors do not accumulate and grow over prolonged simulation periods (Figs. S7 – S15). In general, primary pollutants mainly exhibited positive biases (SO_2 , CO , isoprene) while oxidants mainly exhibited negative biases (OH , H_2O_2). NO_2 and NO biases were initially negative and then resumed positive after the first simulation day, reflecting the dual nature of NO_x production

and consumption in daytime chemistry. Secondary pollutants HNO_3 and PAN exhibited similarly mixed bias patterns as well.

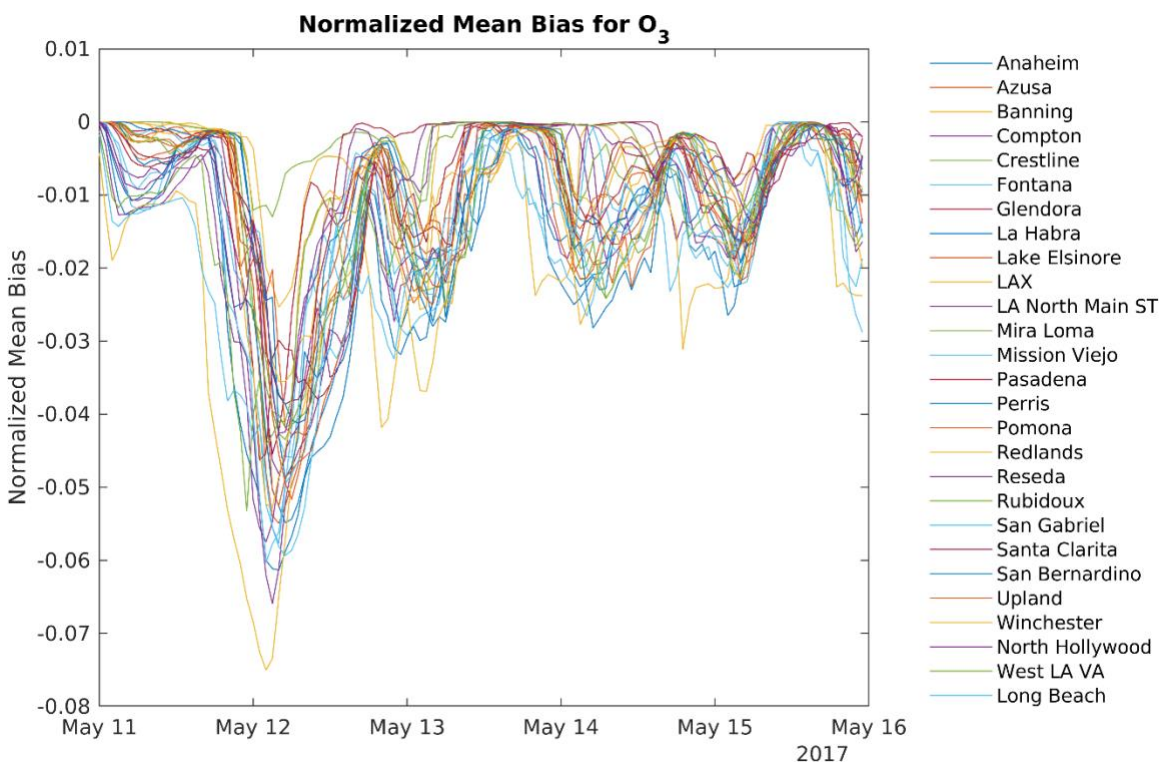


Figure 6. O₃ normalized mean bias for 27 locations over Southern California.

Furthermore, we conducted a performance comparison for CMAQ-GPU across the 10 vertical layers closest to the surface. CMAQ-GPU demonstrates negative normalized mean bias (NMB) values for O₃ concentrations across all sites in Southern California. The highest observed error is -1.9%, as highlighted in Table S2. Figure 7 shows the NMB from the first five vertical layers, while Figure S16 illustrates the next five layers for ozone concentrations. The NMBs exhibit a cyclical and decreasing negative bias over the simulation duration, spanning all layers.

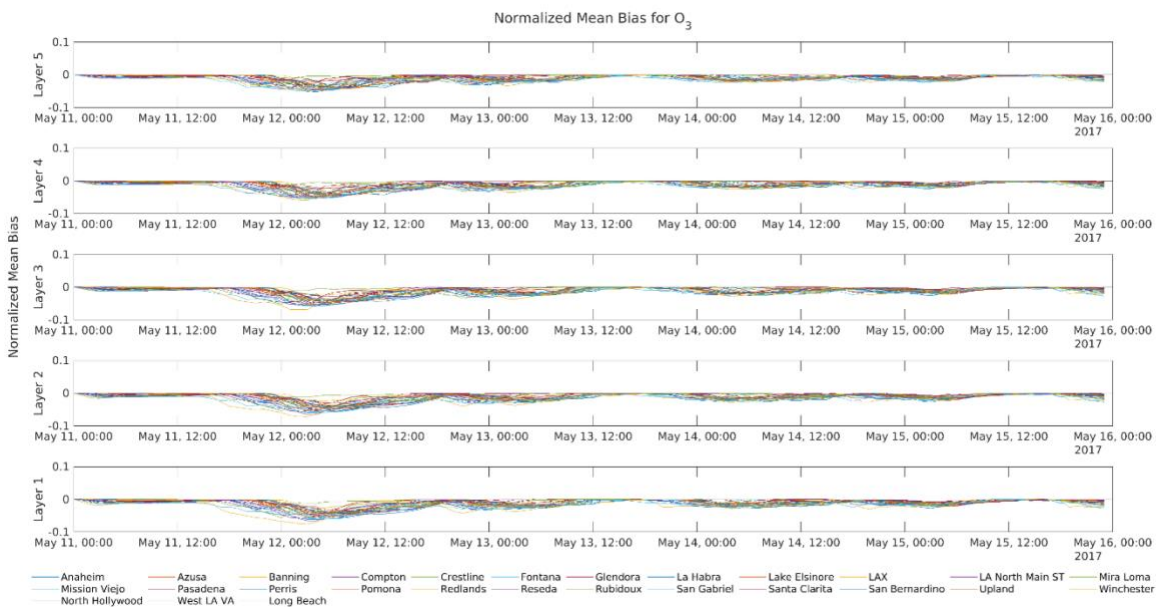


Figure 7. Time series of O_3 normalized mean bias for 27 locations over Southern California for vertical layer 1 to 5.

Discussion

The advantages of GPU implementation for CHEM process solvers include simplification of the compilation process, reduction of the overall model simulation time, and increased readability of the code for future development. However, the CMAQ-CUDA implementation is limited by current computer hardware constraints. The major disadvantage of GPU computing with the current technology is the data transfer time between the host and the device. Even though the GPU kernel performs much faster than the CPU for parallel applications, the movement and reallocation of data can offset any gains from the GPU kernel. The data transfer time can sometimes be even greater than the actual computing time. The bottleneck comes from the PCIe bandwidth limitation, system memory speed, and GPU memory speed. Future releases of newer hardware will lift the bottleneck limitation for GPU computing. Table S3 displays current and future generations of the PCIe bus architecture, where the data transfer rate and bandwidth double with each new generation. It is estimated that the last generation listed in Table S3 will be an eight-fold increase over PCIe 4.0 generation used in the results reported here.

Furthermore, the differences in hardware architecture could cause small numerical discrepancies. Numerical discrepancies between CPUs and GPUs are reduced by merging double-precision multiplication and addition into double-precision fused multiply-add (FMA) architectures to improve accuracy, thereby reducing rounding and preventing subtractive cancellation (39–41). Calculation errors from the differences between GPU and CPU architectures will not be significant because both support double-precision arithmetic. As an added caution, end-users of these models should enable compiler options that enable IEEE arithmetic (42, 43). Nevertheless, dealing with extremely small values for species concentrations will magnify the errors for such species relative to those with larger concentration values because of the L2 norm used in the convergence criterion of CMAQ. For CMAQ-GPU implementation, the best precision to be expected for species concentrations is of the order of 2 to 3 significant figures, as is discussed in Section 5.3 of (44).

Another issue contributing to the discrepancies between CMAQ and CMAQ-CUDA lies in the solver algorithms developed for CPU and GPU architectures. In the original ROS3 solver, each species is solved sequentially, despite any order dependencies. However, our development involved crafting a highly parallel algorithm meticulously designed to maximize loop vectorization and optimize GPU computation. For example, the dot product of two vectors $\mathbf{a} \cdot \mathbf{b}$ is $a_1b_1 + a_2b_2 + a_3b_3 + \dots + a_{n-1}b_{n-1} + a_nb_n$. While the CPU computes the dot product sequentially by calculating $a_1b_1 + a_2b_2$, then adding a_3b_3 to the previous results, the GPU performs the dot product using parallel reduction which combines an array of elements to produce a single value. The GPU computes concurrently every pair of $a_ib_i + a_{i+1}b_{i+1}$. The differences in addition order accumulate, contributing to the rounding error of the two methods.

Additionally, the solution for the ODEs must go back and forth in the Rosenbrock solver more than six times until the numerical solution meets a set of criteria. With CMAQ-CUDA v2.0, the solution from the kernel has to copy to the host for the convergence check and upload to the device again for the next iteration. The disadvantage of the method is that the size of each copy of data is large and requires more GPU memory. For CMAQ-CUDA v1.0, each copy of data requires 3.5 GB of memory and is flushed after the kernel is finished. For CMAQ-CUDA v2.0, each copy of data

requires 6.7 GB of memory. If launching three .cuf kernels in parallel, the amount of data exceeds 20 GB when dealing with a large BLKSIZE. NVIDIA's latest GPU for data centers offers an impressive 48 GB of memory with a sizable increase in cost that would resolve this issue.

In future work, we will introduce CMAQ-CUDA_{v3.0} to overcome this limitation. Implementing CMAQ-CUDA_{v3.0} will migrate the convergence check of the solver onto the kernel to further optimize the transferring time as shown schematically in Figure S5. In this future configuration, the outputs from the kernel are the final solution and reduce the transfer time by a factor of five. This version will optimize the number of selected variables that are needed for the GPU kernel computation. The constant data, such as reaction rates, will be stored on the GPU memory permanently.

Conclusion

Our results from CMAQ-CUDA_{v2.0} show a promising future of GPU computing for CTMs as demonstrated in the CMAQ model implementation. An optimized kernel significantly reduces the computation time for large data sizes. The actual computation time from the GPU kernel is much faster than on the CPU. However, the time for moving the data between the CPU host and the GPU device added a significant amount of time to the overall results. We proposed the CMAQ-CUDA_{v3.0} algorithm to minimize the transfer time by migrating the convergence check loop onto the GPU kernel. The current limitations of our test system are the PCIe bandwidth and memory speed bottleneck. In the future, with the newer generation of PCIe interface and double data rate memory, we will see remarkable improvements in GPU computing for scientific applications. The development of CMAQ-CUDA provided the framework for GPU computing within the CMAQ framework, in which newly developed and highly parallel computing for science process modules can be easily written for GPUs and compiled using the one-step compilation method for Fortran modules and CUDA kernels. End-users may enable or disable GPU computing options with a flag in the build scripts to study gains in performance when compared to the CPU-only host system.

METHODS

CMAQ ODE solvers

Three ordinary differential equation (ODE) solvers are available in CMAQ. These are Euler Backward Iteration (EBI), Rosenbrock (ROS3), and Sparse Matrix Vectorized Gear (SMVGEAR) (EPA, 2019); for a brief overview of these algorithms see Press et al. (1992) (26). The default solver method in CMAQ is EBI due to its lower wall clock computing time. However, EBI is prone to inaccurate results and convergence errors with small time steps for stiff differential equations (26). On the other hand, SMVGEAR has the most accurate results (3). However, the prolonged computing time of the Gear method is a drawback. An example is shown in Figure 8 where the overall CMAQ simulation time for all three solvers with different MPI thread counts is shown. EBI is 2.5x faster than Gear and 2.1x faster than the Rosenbrock solver. Increasing the number of MPI processes improves the overall simulation time; however, the time differences between the solvers remain similar. Section S3, SI Appendix further summarizes mathematical derivations of the solvers.

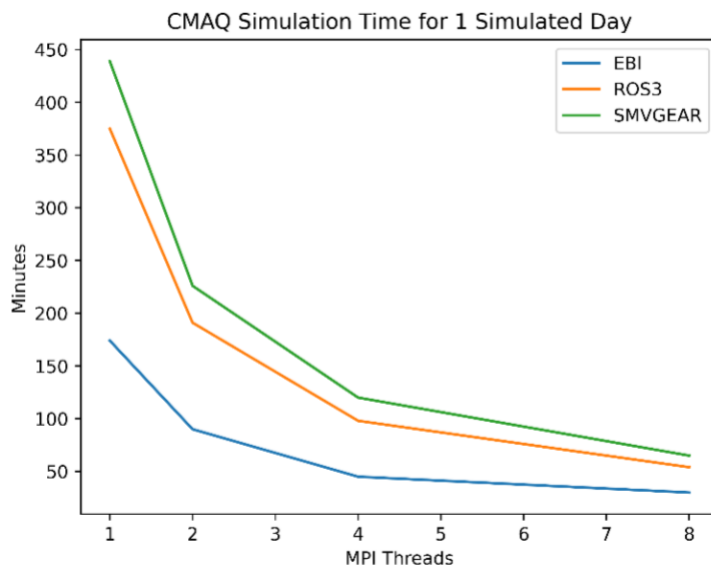


Figure 8. CMAQ simulation time for one simulated date was carried out using EBI (blue), ROS3 (orange), and SMVGEAR (green) solvers with varying numbers of MPI threads.

CMAQ-CUDA Compilation steps

Since CMAQ is written in Fortran, it may be compiled with either Intel Fortran or the open-source GNU Fortran compiler. The CMAQ compilation process is straightforward, with appropriate pre-installed library dependencies. The migration of CMAQ subroutines onto the GPU requires heterogeneous compilers, in which a Fortran compiler is used to compile traditional CMAQ modules (.F files), and nvfortran in the NVIDIA software development kit is used to compile CUDA subroutines (.cuf files). The data flow between .F and .cuf subroutines is strictly enforced, in which .cuf subroutines cannot directly inherit variables from CMAQ data modules.

Parallelization of independent loops

Parallelizing dependent loops results in inaccurate outputs. In gas-phase chemistry, concentrations of several species must be computed in priority. For example, in the EBI method, the concentrations of NO₂, NO, O₃, and O₃P need to be calculated first before computing HO, HO₂, HONO, and HNO₄. In the ROS3 method, the order of the decomposition loop needs to execute in series. Therefore, performing loop-dependent analysis before migrating to the GPU is essential to maintain the model's integrity. We used Bernstein's conditions to test for statements or operations that can be interchanged without altering the model's outputs. The conditions state that if neither Equation 3 to Equation 5 holds, the statements can be interchangeable.

$$OUT_1 \cap IN_2 = \emptyset \quad (3)$$

$$IN_1 \cap OUT_2 = \emptyset \quad (4)$$

$$OUT_1 \cap OUT_2 = \emptyset \quad (5)$$

where IN and OUT are the inputs and outputs, respectively, of tasks 1 and 2.

GPU computing

We developed a single-step compilation of CMAQ's CCTM module (Section S1, SI Appendix) by embedding CUDA Fortran into the original Makefile, in which the original CMAQ modules are compiled with the GNU (45) or Intel (46) compilers, and CUDA subroutines are compiled with CUDA

Fortran. A GPU may be viewed as a complete computing unit with its own instruction sets, ALUs, GPU cache, and GPU memory. The GPU device communicates with the CPU host through a PCIe connection (Figure 9). To carry out an operation of a GPU, three steps need to be followed:

- (1) send a copy of the data from the CPU host to the GPU device,
- (2) launch a CUDA kernel (.cuf) for instruction to compute on the GPU, and
- (3) send the GPU-computed data (results) from the GPU device to the CPU host.

Each step adds to the overall computing time of the system. The general limitation of GPU computing is the bottleneck of the PCIe bandwidth for data transfer between the host and the device.

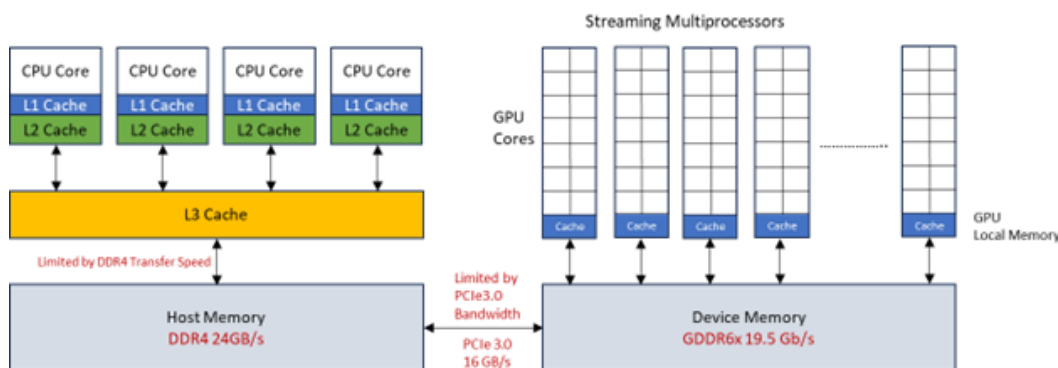


Figure 9. Scheme of a computer with a GPU.

System configuration

The simulations from CMAQ and CMAQ-CUDA were carried out on a consumer desktop computer with an Intel Core i5 8400, 16 GB of system memory, and the NVIDIA RTX 3090 GPU. We used a lower-end computer to ensure the performance of CMAQ on a wide range of devices, including high-performance computers and regular desktops with upgraded graphics cards. The CMAQ modeling domain over Southern California with 4 x 4 km horizontal spacing consists of 156 x 102 x 11 grid cells. The input meteorological data for the CMAQ simulation were the North American Mesoscale Forecast System (NAM) integrated with NOAA high-resolution sea surface temperature (SST). We used OBSGRID (47) to improve meteorological analyses, incorporating the observed

surface and upper air to correct the NAM data corresponding to the ds461(48) and ds351(49) datasets, respectively. Other specifications are summarized in a preceding study (5).

Data Availability

The CMAQ-CUDA code and datasets generated and/or analysed during the current study are available in the GitHub (<https://github.com/kdo037/ROS3-CUDA>) and Zenodo (<https://zenodo.org/record/8274630>) repositories, respectively.

Acknowledgments

The authors thank Prithviraj Yuvaraj for his contribution to the research. This paper was prepared as a result of work sponsored and paid for, in whole or in part, by the Computational and Data-Enabled Science and Engineering from the National Science Foundation Computational Data Science and Engineering Program and the Division of Chemical, Bioengineering, Environmental and Transport Systems (CBET 2053560). The opinions, findings, conclusions, and recommendations are those of the authors and do not necessarily represent the views of the Computational Data Science and Engineering Program.

References

1. R. G. Lamb, J. H. Seinfeld, Mathematical modeling of urban air pollution. General theory. *Environ. Sci. Technol.* **7**, 253–261 (1973).
2. A. Russell, R. Dennis, NARSTO critical review of photochemical models and modeling. *Atmospheric Environment* **34**, 2283–2324 (2000).
3. U.S. EPA, “CMAQv5.2 Operational Guidance Document” (2017).
4. A. Haurie, J. J. E. Kübler, A. Clappier, H. V. D. Bergh, A metamodeling approach for integrated assessment of air quality policies. *Environmental Modeling and Assessment* **9** (2004).
5. K. Do, *et al.*, Emerging investigator series: a machine learning approach to quantify the impact of meteorology on tropospheric ozone in the inland southern California. *Environmental Science: Atmospheres* (2023) <https://doi.org/10.1039/d2ea00077f>.
6. K. M. Foley, *et al.*, Dynamic evaluation of CMAQ part I: Separating the effects of changing emissions and changing meteorology on ozone levels between 2002 and 2005 in the eastern US. *Atmospheric Environment* **103**, 247–255 (2015).
7. Y. Kim, J. S. Fu, T. L. Miller, Improving ozone modeling in complex terrain at a fine grid resolution - Part II: Influence of schemes in MM5 on daily maximum 8-h ozone concentrations and RRFs (Relative Reduction Factors) for SIPs in the non-attainment areas. *Atmospheric Environment* **44** (2010).
8. S. Yu, *et al.*, Evaluation of real-time PM_{2.5} forecasts and process analysis for PM_{2.5} formation over the eastern United States using the Eta-CMAQ forecast model during the 2004 ICARTT study. *J. Geophys. Res.* **113**, D06204 (2008).
9. C. E. Ivey, H. A. Holmes, Y. T. Hu, J. A. Mulholland, A. G. Russell, Development of PM_{2.5} source impact spatial fields using a hybrid source apportionment air quality model. *Geoscientific Model Development* **8**, 2153–2165 (2015).
10. C. E. Ivey, S. Balachandran, S. Colgan, Y. Hu, H. A. Holmes, Investigating fine particulate matter sources in Salt Lake City during persistent cold air pool events. *Atmospheric Environment* **213**, 568–578 (2019).
11. H. Simon, K. R. Baker, S. Phillips, *Compilation and interpretation of photochemical model performance statistics published between 2006 and 2012* (2012).
12. C. Cai, J. T. Kelly, J. C. Avise, A. P. Kaduwela, W. R. Stockwell, Photochemical Modeling in California with Two Chemical Mechanisms: Model Intercomparison and Response to Emission Reductions. *Journal of the Air & Waste Management Association* **61**, 559–572 (2011).
13. F. Garcia–Menendez, A. Yano, Y. Hu, M. Talat Odman, An adaptive grid version of CMAQ for improving the resolution of plumes. *Atmospheric Pollution Research* **1**, 239–249 (2010).
14. D. J. Luecken, G. Yarwood, W. T. Hutzell, Multipollutant modeling of ozone, reactive nitrogen and HAPs across the continental US with CMAQ-CB6. *Atmospheric Environment* **201**, 62–72 (2019).

15. K. W. Appel, *et al.*, The Community Multiscale Air Quality (CMAQ) model versions 5.3 and 5.3.1: system updates and evaluation. *Geosci. Model Dev.* **14**, 2867–2897 (2021).
16. A. Pouyaei, Y. Choi, J. Jung, B. Sadeghi, C. H. Song, Concentration Trajectory Route of Air pollution with an Integrated Lagrangian model (C-TRAIL Model v1.0) derived from the Community Multiscale Air Quality Model (CMAQ Model v5.2). *Geoscientific Model Development* **13**, 3489–3505 (2020).
17. G. Sarwar, D. Luecken, G. Yarwood, G. Z. Whitten, W. P. L. Carter, Impact of an updated carbon bond mechanism on predictions from the CMAQ modeling system: Preliminary assessment. *Journal of Applied Meteorology and Climatology* **47**, 3–14 (2008).
18. W. T. Hutzell, D. J. Luecken, K. W. Appel, W. P. L. Carter, Interpreting predictions from the SAPRC07 mechanism based on regional and continental simulations. *Atmospheric Environment* **46**, 417–429 (2012).
19. W. P. L. Carter, Development of the SAPRC-07 chemical mechanism. *Atmospheric Environment* **44**, 5324–5335 (2010).
20. W. P. L. Carter, “DOCUMENTATION OF THE SAPRC-22 MECHANISM” (2023).
21. L. Clarke, I. Glendinning, R. Hempel, “The MPI Message Passing Interface Standard” in *Programming Environments for Massively Parallel Distributed Systems*, K. M. Decker, R. M. Rehmann, Eds. (Birkhäuser Basel, 1994), pp. 213–218.
22. W. Gropp, E. Lusk, N. Doss, A. Skjellum, A high-performance, portable implementation of the MPI message passing interface standard. *Parallel Computing* **22** (1996).
23. E. Lusk, S. Huss, B. Saphir, M. Snir, MPI: A message-passing interface standard Version 3.0. *International Journal of Supercomputer Applications* **8** (2009).
24. D. C. Wong, *et al.*, WRF-CMAQ two-way coupled system with aerosol feedback: Software development and preliminary results. *Geoscientific Model Development* (2012) <https://doi.org/10.5194/gmd-5-299-2012>.
25. E. Hairer, G. Wanner, *Solving Ordinary Differential Equations II Stiff and Differential-Algebraic Problems*, 2nd Ed. (Springer, 1996).
26. W. H. Press, B. P. Flannery, S. A. Teukolsky, W. T. Vetterling, *Numerical Recipes in FORTRAN 77: Volume 1, Volume 1 of Fortran Numerical Recipes* (1992).
27. C. W. Gear, *Numerical initial value problems in ordinary differential equations* (Prentice-Hall, 1971).
28. M. Z. Jacobson, R. P. Turco, SMVGEAR: A sparse-matrix, vectorized gear code for atmospheric models. *Atmospheric Environment* **28** (1994).
29. NVIDIA, Whitepaper NVIDIA’s Next Generation CUDA Compute Architecture. *ReVision* **23** (2009).
30. N. Whitehead, A. Fit-Florea, Precision & performance: Floating point and IEEE 754 compliance for NVIDIA GPUs. *m (A+ B)* **21**, 18749–19424 (2011).

31. M. Guevara, C. Gregg, K. Hazelwood, K. Skadron, Enabling Task Parallelism in the CUDA Scheduler in *Workshop on Programming Models for Emerging Architectures*, (Citeseer, 2009), p. 84.
32. G. Delic, Developing CMAQ for many-core and GPGPU processors in *9th Annual CMAS Conference, Chapel Hill, North Carolina, October 11-13*, (2010), pp. 1–6.
33. K. Cao, *et al.*, GPU-HADVPPM V1.0: high-efficient parallel GPU design of the Piecewise Parabolic Method (PPM) for horizontal advection in 2 air quality model (CAMx V6.10) 3. *EGUsphere* (2023) <https://doi.org/10.5194/egusphere-2023-410>.
34. K. Matam, S. R. Krishna Bharadwaj Indarapu, K. Kothapalli, Sparse matrix-matrix multiplication on modern architectures in *2012 19th International Conference on High Performance Computing*, (IEEE, 2012), pp. 1–10.
35. S. Ristov, M. Gusev, G. Velkoski, Optimal block size for matrix multiplication using blocking in *2014 37th International Convention on Information and Communication Technology, Electronics and Microelectronics (MIPRO)*, (IEEE, 2014), pp. 295–300.
36. P. D. Sulatycke, K. Ghose, Caching-efficient multithreaded fast multiplication of sparse matrices in *Proceedings of the First Merged International Parallel Processing Symposium and Symposium on Parallel and Distributed Processing*, (IEEE Comput. Soc, 1998), pp. 117–123.
37. N. Fauzia, L.-N. Pouchet, P. Sadayappan, Characterizing and enhancing global memory data coalescing on GPUs in *2015 IEEE/ACM International Symposium on Code Generation and Optimization (CGO)*, (IEEE, 2015), pp. 12–22.
38. M. Winter, M. Parger, D. Mlakar, M. Steinberger, Are dynamic memory managers on GPUs slow?: a survey and benchmarks in *Proceedings of the 26th ACM SIGPLAN Symposium on Principles and Practice of Parallel Programming*, (ACM, 2021), pp. 219–233.
39. P. Blanchard, N. J. Higham, F. Lopez, T. Mary, S. Pranesh, Mixed precision block fused multiply-add: Error analysis and application to GPU tensor cores. *SIAM Journal on Scientific Computing* **42** (2020).
40. E. Quinell, E. E. Swartzlander, C. Lemonds, Bridge floating-point fused multiply-add design. *IEEE Transactions on Very Large Scale Integration (VLSI) Systems* **16** (2008).
41. H. Zhang, D. Chen, S.-B. Ko, Efficient Multiple-Precision Floating-Point Fused Multiply-Add with Mixed-Precision Support. *IEEE Trans. Comput.* **68**, 1035–1048 (2019).
42. N. J. Higham, *Accuracy and Stability of Numerical Algorithms*, Second (Society for Industrial and Applied Mathematics, 2002) <https://doi.org/10.1137/1.9780898718027> (July 29, 2023).
43. M. L. Overton, *Numerical Computing with IEEE Floating Point Arithmetic* (Society for Industrial and Applied Mathematics, 2001) <https://doi.org/10.1137/1.9780898718072> (July 29, 2023).
44. G. Delic, A Thread Parallel Sparse Matrix Chemistry Algorithm for the Community Multiscale Air Quality Model. *Modern Environmental Science and Engineering* **5**, 775–791 (2019).
45. GNU Fortran, GNU Fortran - GNU Project (July 29, 2023).

46. Intel, Intel | Data Center Solutions, IoT, and PC Innovation (July 29, 2023).
47. R. C. Gilliam, J. E. Pleim, Performance assessment of new land surface and planetary boundary layer physics in the WRF-ARW. *Journal of Applied Meteorology and Climatology* **49** (2010).
48. National Centers for Environmental Prediction, National Weather Service, NOAA, U.S. Department of Commerce, NCEP ADP Global Surface Observational Weather Data, October 1999 - continuing (2004).
49. Satellite Services Division, Office of Satellite Data Processing and Distribution, NESDIS, NOAA, U.S. Department of Commerce, National Centers for Environmental Prediction, National Weather Service, NOAA, U.S. Department of Commerce, NCEP ADP Global Upper Air Observational Weather Data, October 1999 - continuing (2004).

Supporting Information for Graphics Processing Unit Assisted Computation for a Gas-Phase Chemical Solver in a Regulatory Chemical Transport Model

Khanh Do^{1,2}, George Delic³, José M. Rodríguez Borbón⁴, Duncan Quevedo⁵, Bryan M. Wong⁴,
and Cesunica Ivey^{2,5,*}

¹Department of Chemical and Environmental Engineering, University of California, Riverside, CA, 92521

²Center for Environmental Research and Technology, Riverside, CA, 92507

³Hiperism Consulting, LLC, Chapel Hill, NC, 27514

⁴Materials Science and Engineering Program, University of California, Riverside, CA, 92521

⁵Department of Civil and Environmental Engineering, University of California, Berkeley, CA, 94720

*Cesunica E. Ivey, corresponding author

Email: iveyc@berkeley.edu

This PDF file includes:

Supporting text
Figures S1 to S16
Tables S1 to S3
Legends for Software S1
SI References

Other supporting materials for this manuscript include the following:

Software S1

S1. CMAQ Science Processes

CMAQ describes the dynamics of the atmosphere with a set of governing equations on grid cells in terms of the column, row, and layer. Figure S1 shows the simplified overview of CMAQ's modules, in which the science processes operate in series. The science process module calls vertical diffusion (vdiff), horizontal advection (hadv), vertical advection (zadv), horizontal diffusion (hdiff), cloud process (cldproc), and gas-phase chemistry (chem) (1, 2). The first four processes imitate the transport of the model using meteorological data inputs from WRF or other meteorology models. The cloud process computes the concentration changes in the cloud due to aqueous chemistry, scavenging, and wet deposition. The chem process calculates the gas phase concentrations based on the chemical mechanism provided by user input (SAPRC, CB, etc.).

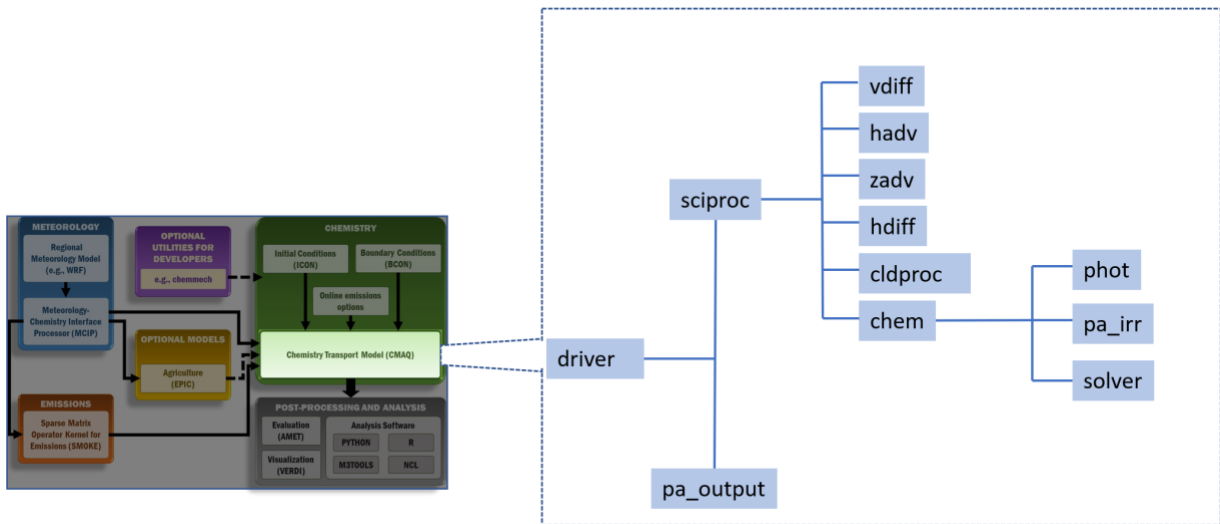


Fig. S1. CMAQ's CCTM science process modules. Source for left-side of diagram: www.epa.gov/cmaq.

S2. Rosenbrock solver for CMAQ-CUDAv1.0

Because the .cuf subroutines (compiled with nvfortran) cannot understand .F routines (compiled with a Fortran compiler), we introduce an intermediate.F subroutine (compiled with nvfortran) that communicates with both .F and .cuf subroutines. Subroutine intermediate.F is the bridge between the CPU host and the GPU device, and most data and variables must pass through intermediate.F. The execution of rbfeval.F, rbjacob.F, rbdecomp.F, and rbsolve.F is repeated until the tolerance criterion is met. It should be observed that the tolerance criterion in CMAQ is an L2 norm of the differences between iterations for each species concentration, and species with larger concentrations are favored over those with smaller values.

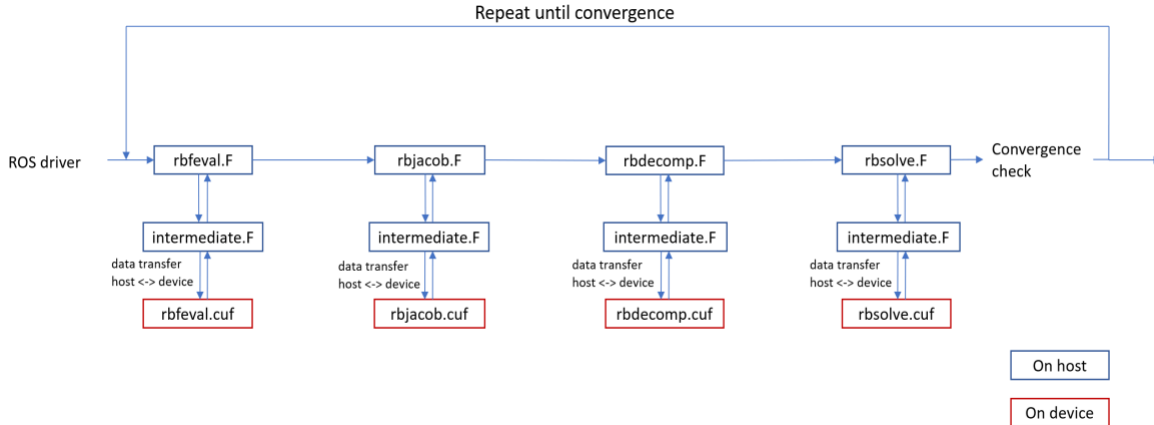


Fig. S2. Rosenbrock solver block diagram for CMAQ-CUDAv1.0 implementation. The blue blocks are executed using the CPU (host), and the red blocks are executed using the GPU (device). Because of the different compilers, .cuf and .F subroutines communicate through intermediate.F.

S3. CMAQ ODE Solver Details

The EBI solver is the default CMAQ method, which is the most commonly used due to its computational efficiency. However, considering its accuracy and data structure, the EBI method is unsuitable for GPU computation. The general differential equations for a chemical system can be expressed in Equation 1, in which the change in concentration of specie i equals the difference between the production and the loss of specie i .

$$\frac{dc_i}{dt} = P_i - L_i c_i \quad \text{and} \quad i = 1, \dots, s \quad (1)$$

where P_i is the production, L_i is the loss term of specie i , and s is the number of chemical species (43). The numerical solution using the EBI approximation is shown as $c_i^{n+1} = c_i^n + P_i^{n+1} \Delta t - L_i^{n+1} \Delta t c_i^{n+1}$, and can be written in the form:

$$c_i^{n+1} = \frac{c_i^n + P_i^{n+1} \Delta t}{1 - L_i^{n+1} \Delta t} \quad (2)$$

The solution using the EBI method is just a simple linear combination, which makes the method effective in solving first-order ODEs. To solve the concentrations in the gas phase, CMAQ iterates Equation 2 through all the gas species until the convergence criteria are met. Because the correct concentrations depend on the order of the species, Equation 2 must be carried out to obtain the correct solution. The EBI method is configured in sequential mode, and porting the EBI solver to the GPU is not beneficial.

The CMAQ Rosenbrock and SMVGEAR solvers are straightforward applications of Gaussian Elimination to decompose a (sparse) matrix into LU form where L and U are lower and upper triangular matrices (44). This version was designed based on the code originally developed by M. Jacobson (28, 43). This approach added a sparse-matrix package and vectorized loops over blocks with grid cells in the grid-cell dimension to improve computational efficiency in vector performance at the instruction level on commodity architectures (Z. Jacobson & Turco, 1994). For a set of ODEs $\frac{dc}{dt} = f(t, c)$, the prediction matrix is $P \cong I - h\beta_o J$, where c is the concentration vector, I is the identity matrix, h is the time step, β is the scalars, and $J = \frac{\partial c}{\partial t}$ is the Jacobian matrix.

The Gear method (27) uses Gaussian decomposition in a direct method (44) with back-substitution to solve for the concentrations. In this method, pivoting is not applied in CMAQ based on the assumption that since the sparse matrix is diagonally dominant, it is safe to do so. Nevertheless, there are potential numerical precision consequences of this choice. This was done in an effort to reduce the time spent in the decomposition where the outer loop needs to be in sequential order and, therefore, cannot be parallelized. The calculation of the Gear method can be carried out independently with matrix and vector operations, has a high degree of parallelization, and favors GPU computation.

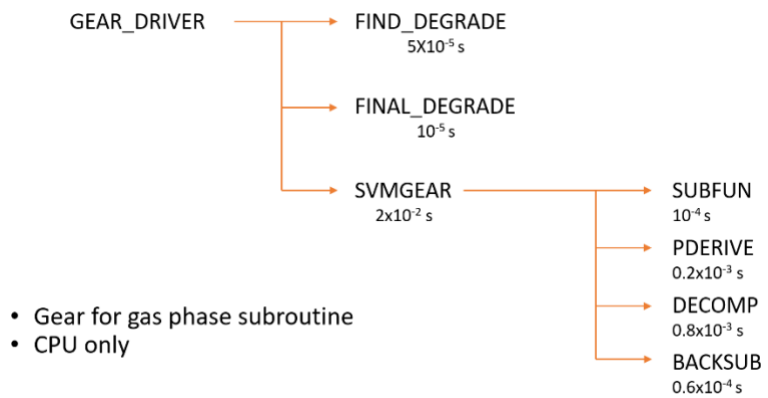


Fig. S3. Timing of GEAR subroutines.

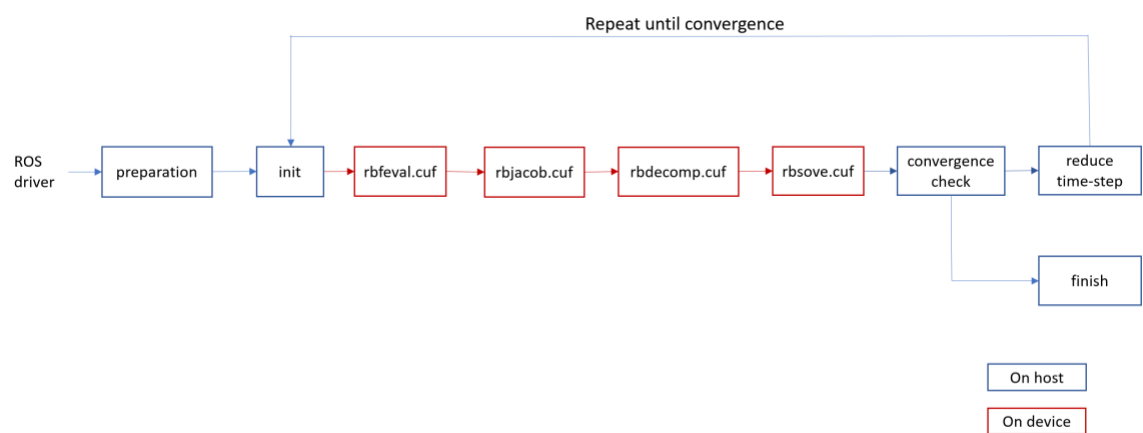


Fig. S4. CUDA Rosenbrock solver block diagram for CMAQ-CUDA_{v2.0}. The blue blocks are executed using the CPU (host), and the red blocks are executed using GPU (device). The four .cuf subroutines (red blocks) operate on the GPU without requiring data transfer with the host between each subroutine.

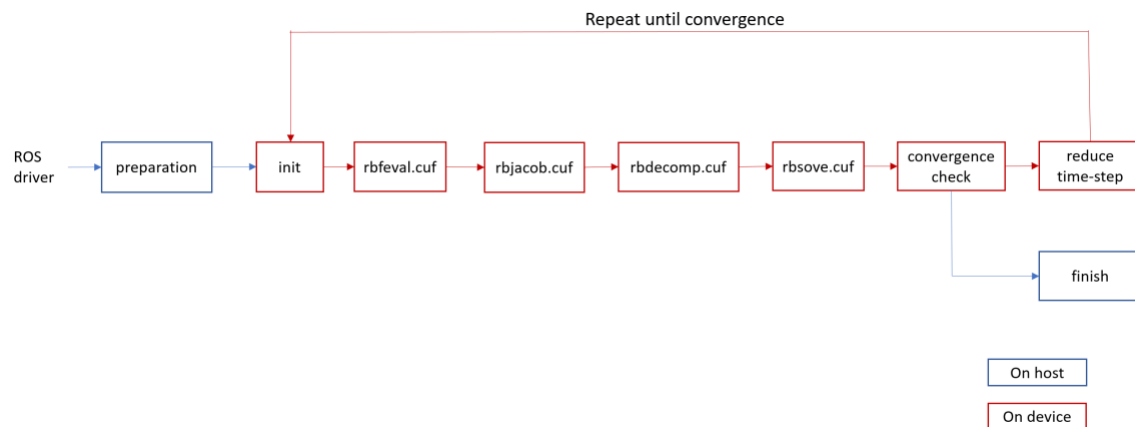


Fig. S5. CUDA Rosenbrock solver block diagram for CMAQ-CUDA v3.0. The blue blocks are executed using the CPU (host), and the red blocks are executed using GPU (device). The convergence check is ported to the kernel to optimize the transferring time. The outputs from the kernel are the final solutions.

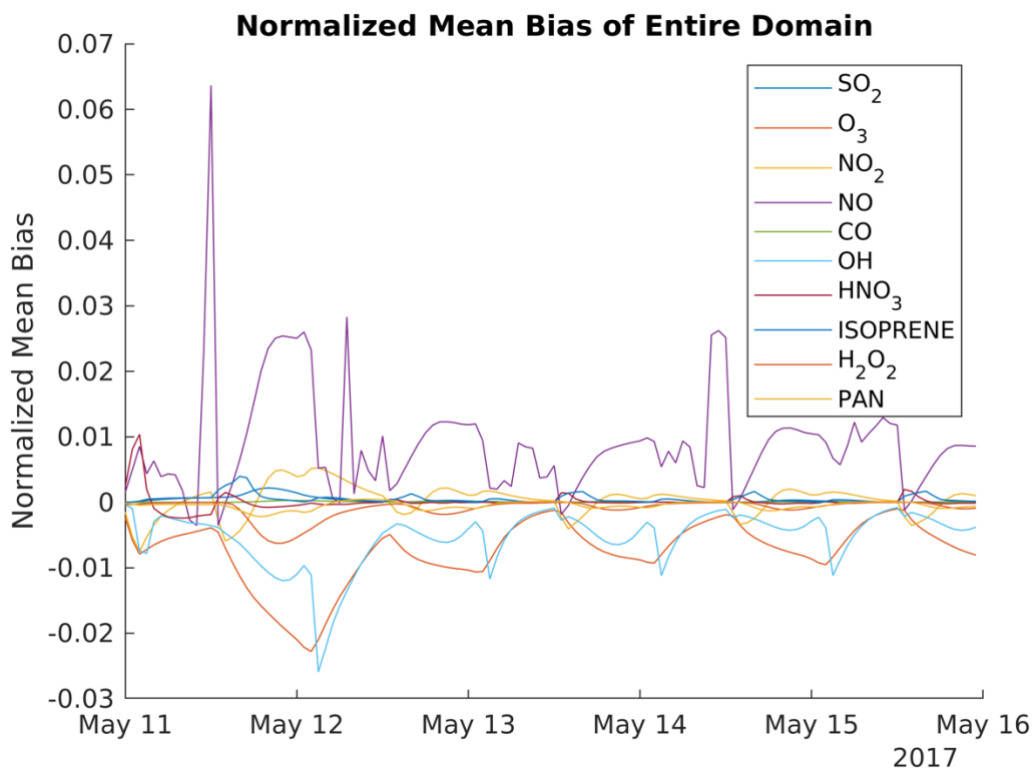


Fig. S6. Normalized mean bias for SO₂, O₃, NO₂, NO, CO, OH, HNO₃, Isoprene, H₂O₂, and PAN for the entire domain.

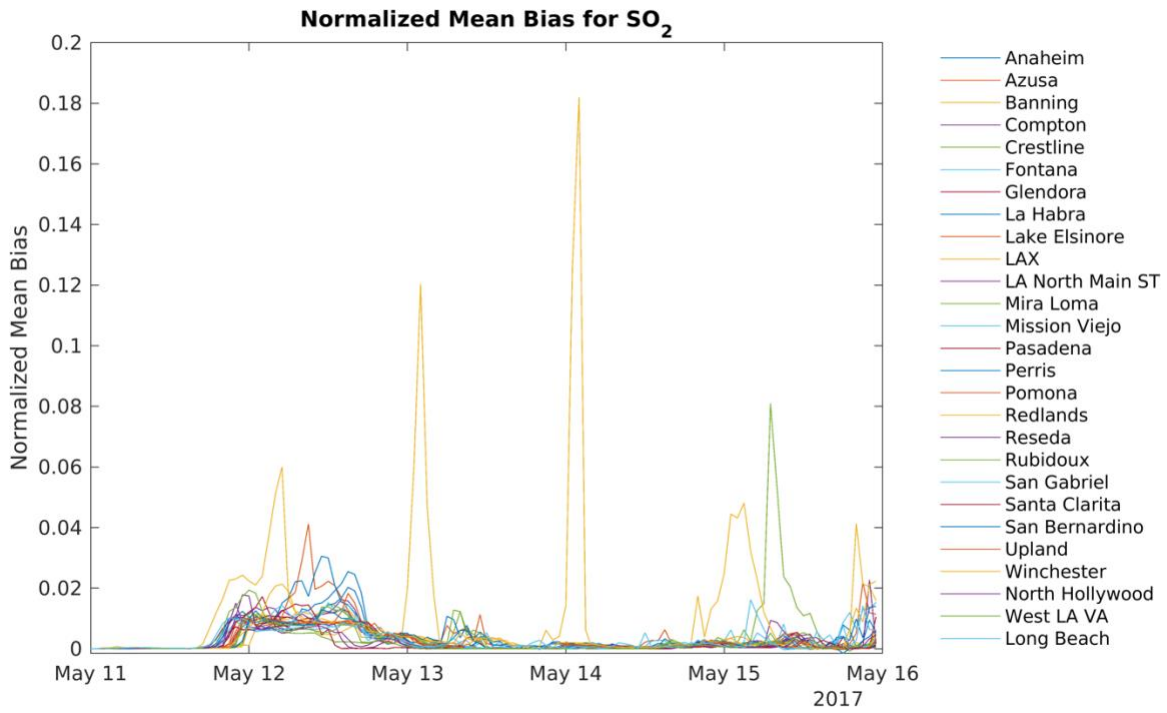


Fig. S7. SO₂ normalized mean bias for 27 locations over Southern California

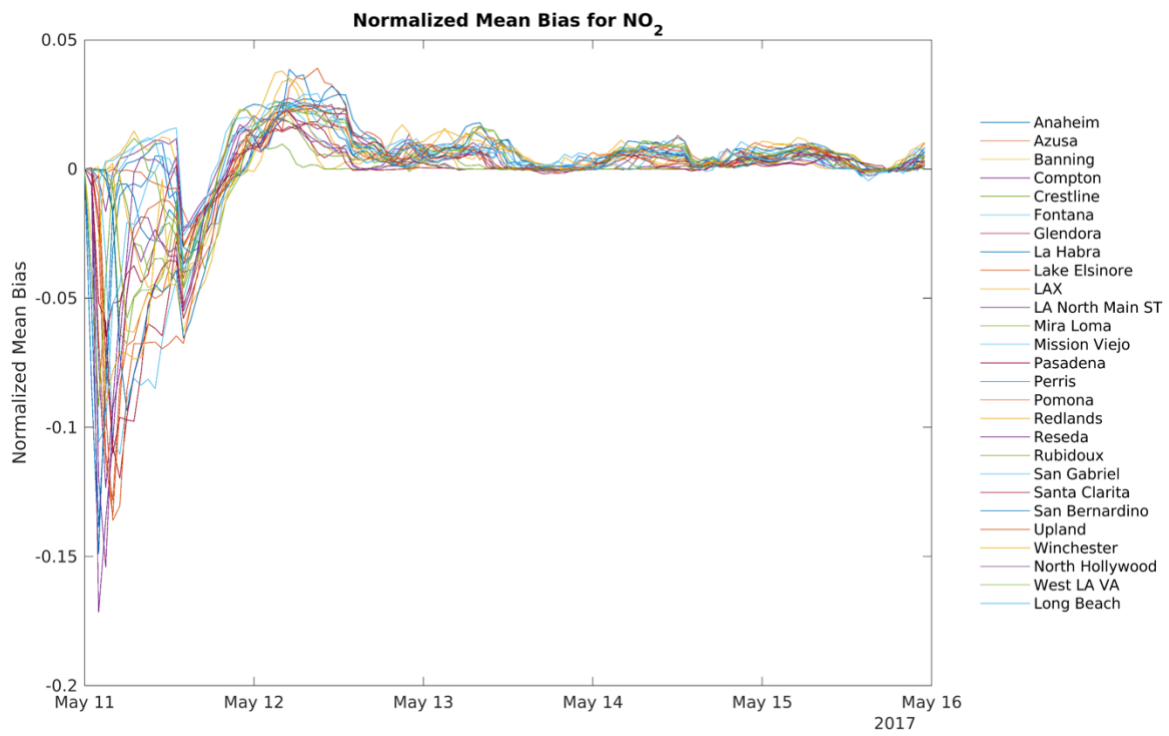


Fig. S8. NO₂ normalized mean bias for 27 locations over Southern California

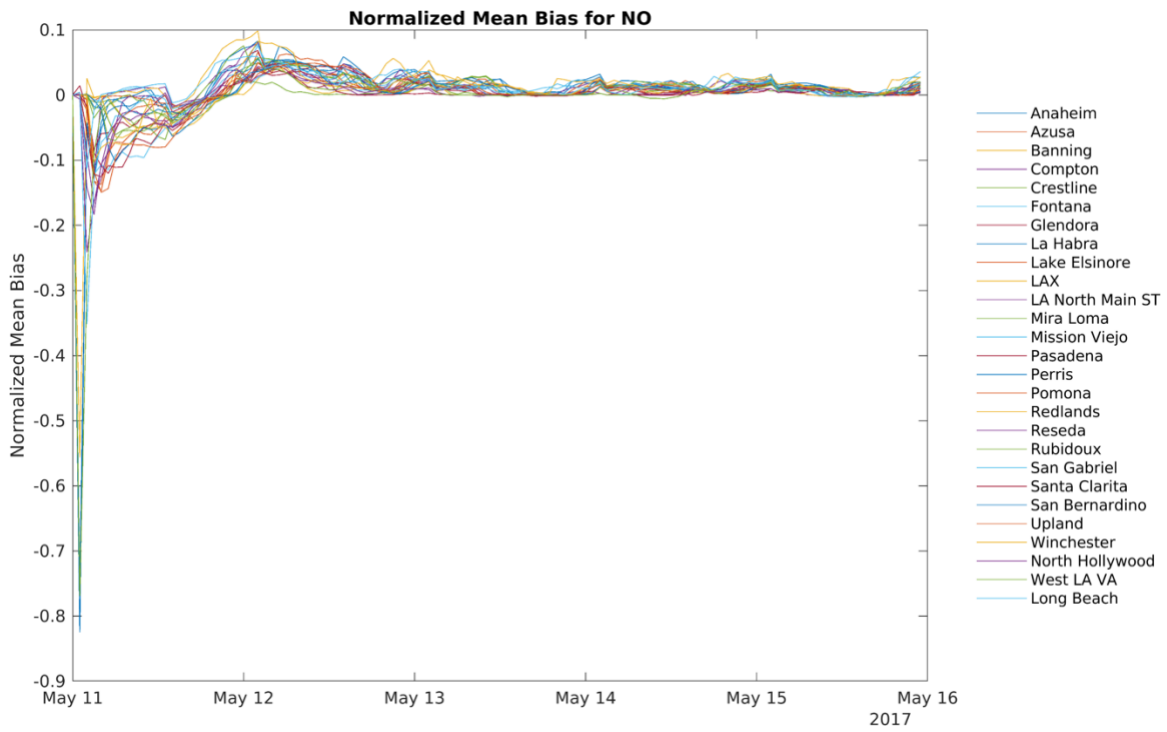


Fig. S9. NO normalized mean bias for 27 locations over Southern California

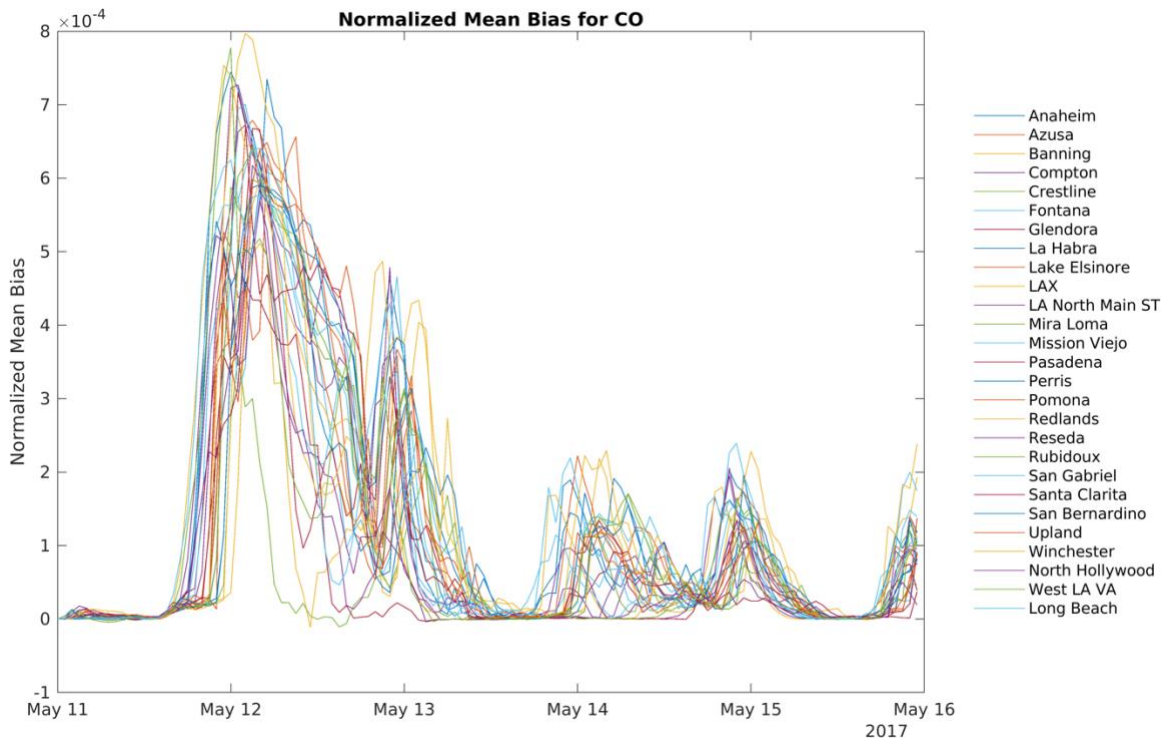


Fig. S10. CO normalized mean bias for 27 locations over Southern California

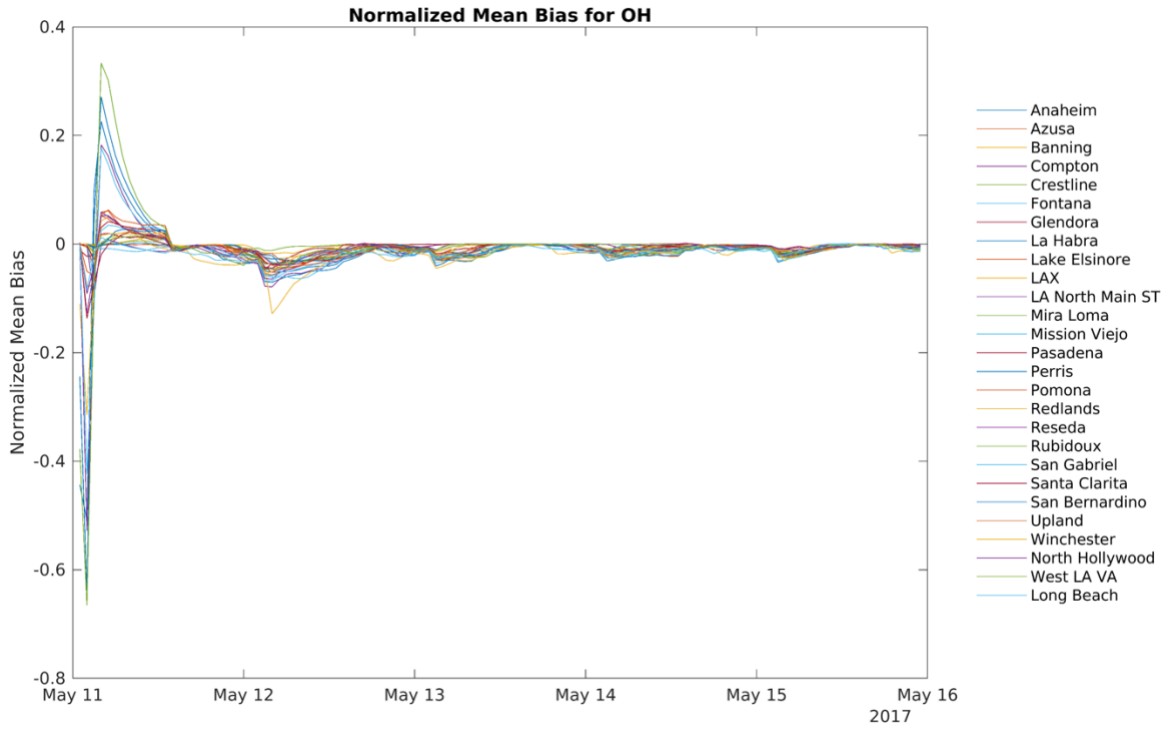


Fig. S11. OH normalized mean bias for 27 locations over Southern California

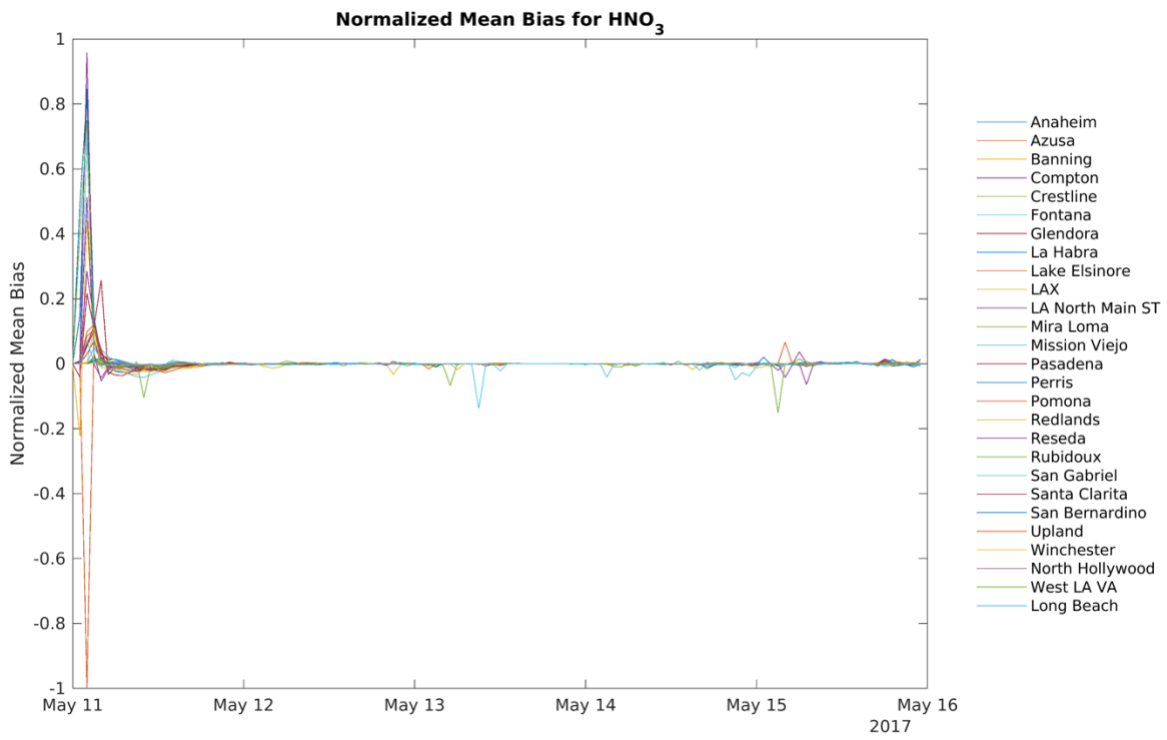


Fig. S12. HNO₃ normalized mean bias for 27 locations over Southern California

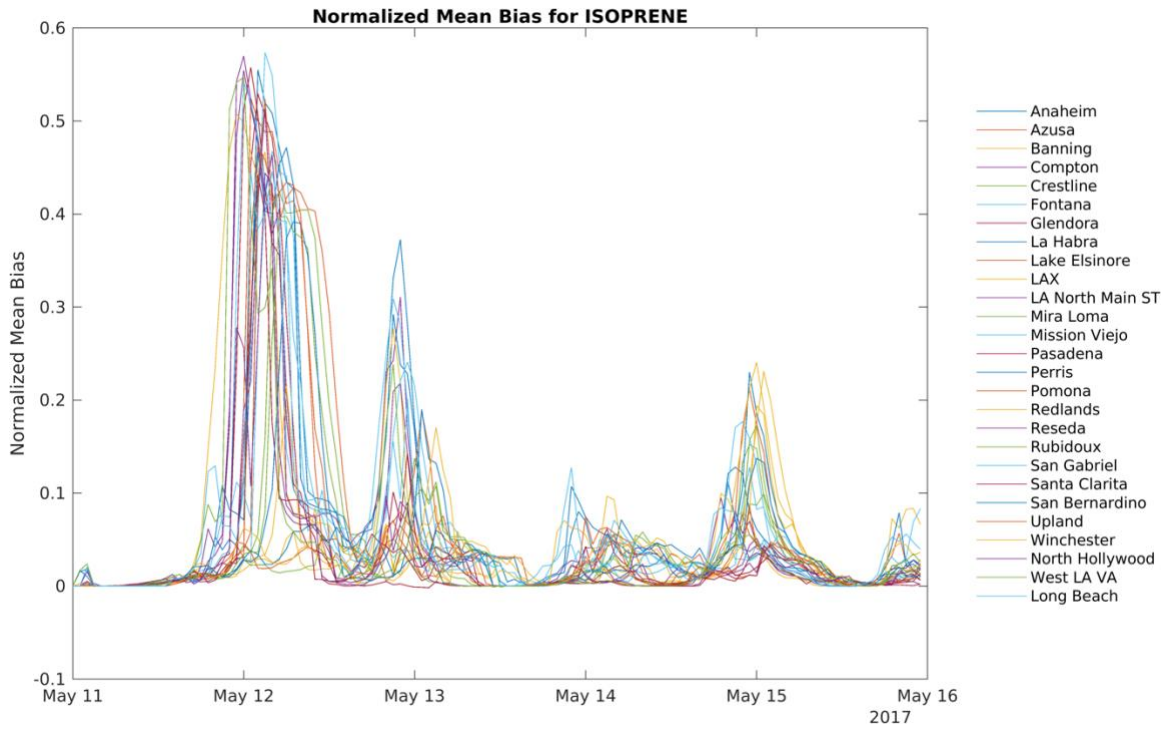


Fig. S13. Isoprene normalized mean bias for 27 locations over Southern California

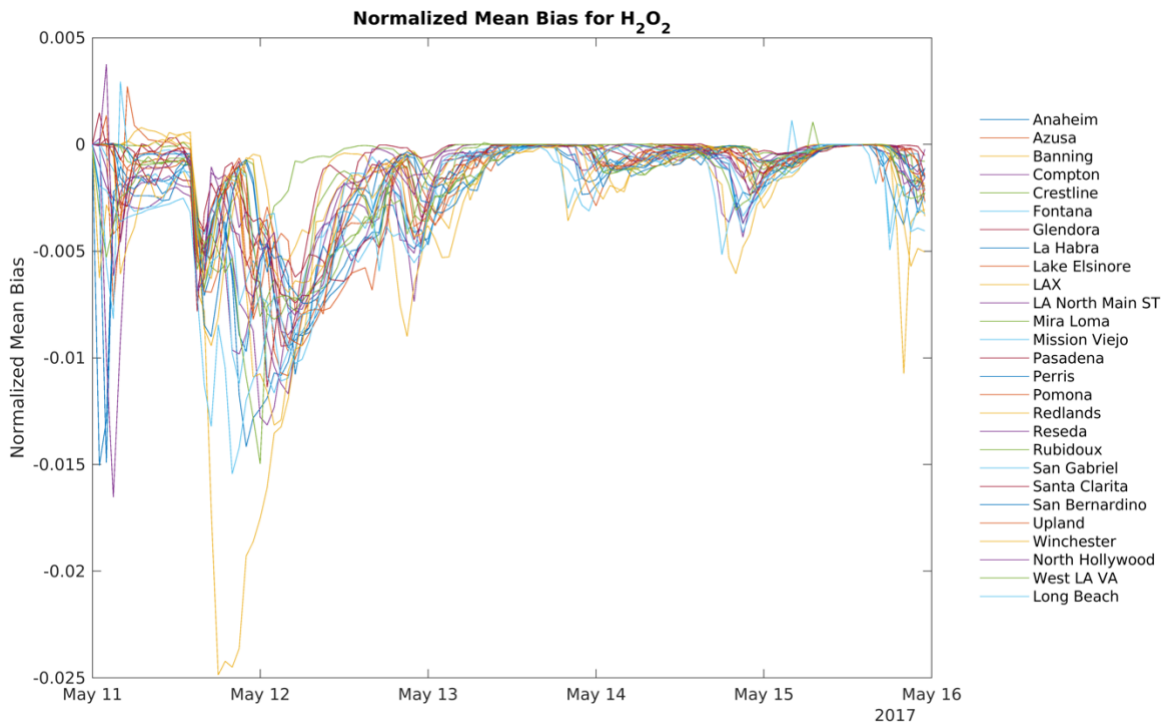


Fig. S14. H₂O₂ normalized mean bias for 27 locations over Southern California

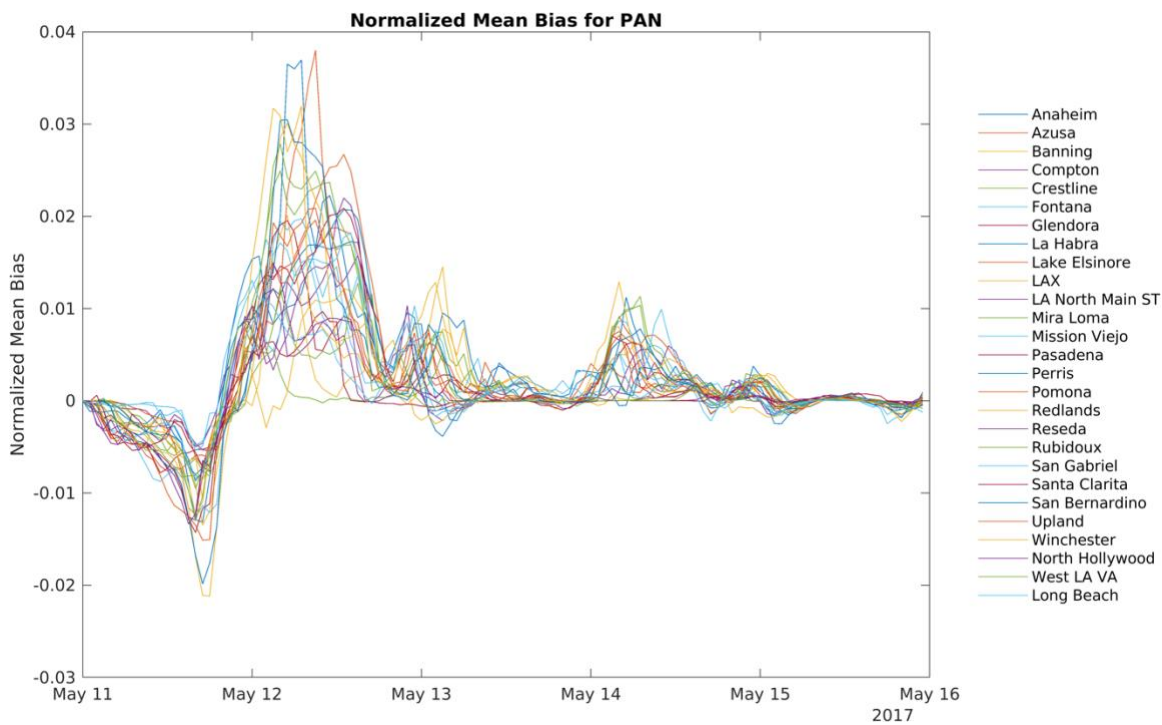


Fig. S15. Peroxyacetyl nitrate (PAN) normalized mean bias for 27 locations over Southern California

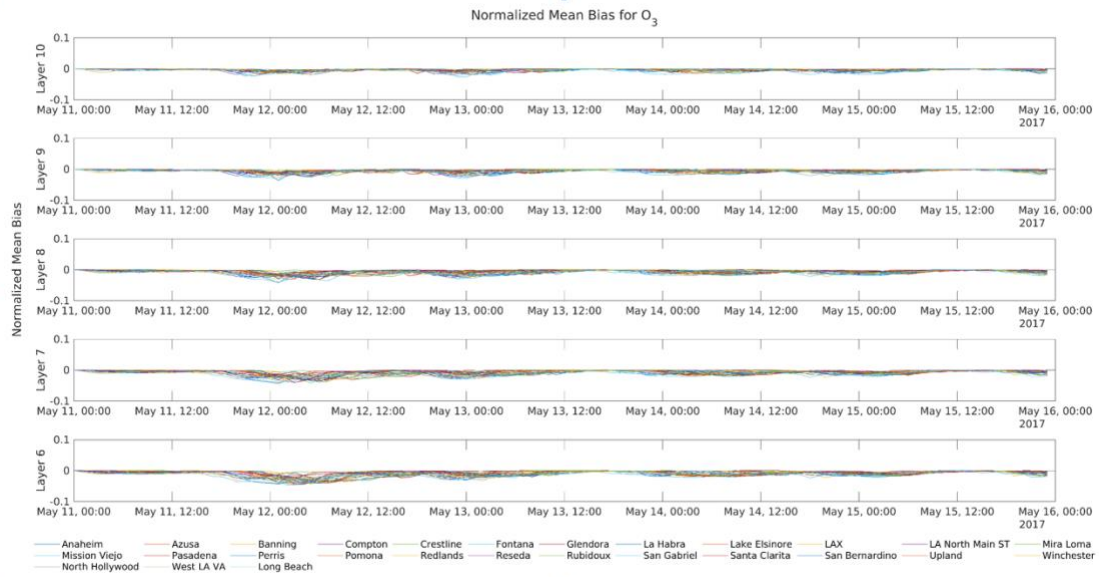


Fig. S16. Time series of O₃ normalized mean bias for 27 locations over Southern California for vertical layer 1 to 5.

Table S1. Computing time for RBFEVAL, RBJACOB, RBCECOMP, and RBSOLVE subroutines for CMAQ and CMAQ-CUDAv1.0. The time was measured in seconds and was the average of a CMAQ timestep for 2,100 and 10,000 BLKSIZE. CTD (copy to device) is the time for transferring data from host to device. CTH (copy to host) is the time for copying the results from the device to the host. KER (kernel) is the GPU computing time in milliseconds.

	RBFEVAL (ms)			RBJACOB (ms)			RBDECOMP (ms)			RBSOLVE (ms)		
	CTD	KER	CTH	CTD	KER	CTH	CTD	KER	CTH	CTD	KER	CTH
CMAQCUDAv1.0 2,100 BLKS	3.8	2.5	0.39	12	14	13	11	11	9.8	9.9	1.6	11
CMAQ 2,100 BLKS	0	4.0	0	0	12	0	0	38	0	0	4.1	0
CMAQCUDAv1.0 10,000 BLKS	24	1.9	1.7	50	7.6	58	53	13	45	46	1.7	53
CMAQ 10,000 BLKS	0	23	0	0	56	0	0	190	0	0	21	0

Table S2. O₃ normalized mean bias for 27 locations over Southern California for 10 vertical layers near the surface, averaged over May 11-16, 2017.

Layers	1	2	3	4	5	6	7	8	9	10
Anaheim	-0.0181	-0.0180	-0.0174	-0.0163	-0.0149	-0.0132	-0.0110	-0.0089	-0.0065	-0.0045
Azusa	-0.0102	-0.0104	-0.0105	-0.0105	-0.0102	-0.0096	-0.0083	-0.0067	-0.0051	-0.0034
Banning	-0.0057	-0.0056	-0.0054	-0.0050	-0.0044	-0.0037	-0.0033	-0.0029	-0.0025	-0.0021
Compton	-0.0158	-0.0158	-0.0153	-0.0143	-0.0129	-0.0112	-0.0099	-0.0085	-0.0064	-0.0048
Crestline	-0.0034	-0.0033	-0.0032	-0.0029	-0.0025	-0.0022	-0.0017	-0.0014	-0.0012	-0.0011
Fontana	-0.0092	-0.0094	-0.0096	-0.0094	-0.0089	-0.0080	-0.0069	-0.0059	-0.0044	-0.0031
Glendora	-0.0073	-0.0075	-0.0072	-0.0069	-0.0063	-0.0057	-0.0049	-0.0041	-0.0030	-0.0021
La Habra	-0.0153	-0.0152	-0.0148	-0.0138	-0.0126	-0.0112	-0.0096	-0.0080	-0.0064	-0.0045
Lake Elsinore	-0.0118	-0.0115	-0.0111	-0.0100	-0.0091	-0.0077	-0.0062	-0.0048	-0.0037	-0.0028
LAX	-0.0190	-0.0174	-0.0157	-0.0139	-0.0124	-0.0107	-0.0092	-0.0076	-0.0061	-0.0047
LA N Main St	-0.0135	-0.0134	-0.0131	-0.0123	-0.0111	-0.0099	-0.0088	-0.0075	-0.0056	-0.0042
Mira Loma	-0.0119	-0.0118	-0.0117	-0.0113	-0.0106	-0.0098	-0.0085	-0.0065	-0.0045	-0.0031
Mission Viejo	-0.0153	-0.0153	-0.0152	-0.0147	-0.0139	-0.0127	-0.0112	-0.0095	-0.0079	-0.0063
Pasadena	-0.0111	-0.0110	-0.0106	-0.0099	-0.0090	-0.0081	-0.0069	-0.0058	-0.0045	-0.0035
Perris	-0.0121	-0.0119	-0.0114	-0.0102	-0.0089	-0.0074	-0.0062	-0.0051	-0.0041	-0.0032
Pomona	-0.0126	-0.0126	-0.0124	-0.0118	-0.0110	-0.0098	-0.0082	-0.0068	-0.0048	-0.0029
Redlands	-0.0076	-0.0077	-0.0076	-0.0075	-0.0069	-0.0060	-0.0049	-0.0040	-0.0033	-0.0028
Reseda	-0.0063	-0.0062	-0.0060	-0.0058	-0.0054	-0.0050	-0.0043	-0.0035	-0.0028	-0.0022
Rubidoux	-0.0112	-0.0113	-0.0112	-0.0108	-0.0102	-0.0093	-0.0080	-0.0061	-0.0040	-0.0029
San Gabriel	-0.0140	-0.0138	-0.0132	-0.0122	-0.0110	-0.0094	-0.0079	-0.0067	-0.0053	-0.0039
Santa Clarita	-0.0051	-0.0051	-0.0049	-0.0045	-0.0042	-0.0039	-0.0034	-0.0028	-0.0023	-0.0019
SB	-0.0089	-0.0089	-0.0090	-0.0088	-0.0082	-0.0076	-0.0068	-0.0059	-0.0047	-0.0036
Upland	-0.0090	-0.0091	-0.0091	-0.0087	-0.0081	-0.0071	-0.0062	-0.0050	-0.0036	-0.0027
Winchester	-0.0124	-0.0123	-0.0121	-0.0116	-0.0109	-0.0099	-0.0085	-0.0068	-0.0050	-0.0034
N. Hollywood	-0.0075	-0.0075	-0.0073	-0.0071	-0.0067	-0.0061	-0.0055	-0.0048	-0.0038	-0.0030
West LA VA	-0.0105	-0.0103	-0.0101	-0.0095	-0.0088	-0.0078	-0.0066	-0.0054	-0.0039	-0.0028
Long Beach	-0.0178	-0.0176	-0.0171	-0.0163	-0.0151	-0.0136	-0.0119	-0.0102	-0.0078	-0.0060

Table S3. Improvement of data transfer rate over PCIe generations.

Generation	Year of Release	Data Transfer Rate	Bandwidth x1	Bandwidth x16
PCIe 3.0	2010	8.0 GT/s	1.0 GB/s	16 GB/s
PCIe 4.0	2017	16.0 GT/s	2.0 GB/s	32 GB/s
PCIe 5.0	2019	32.0 GT/s	4.0 GB/s	64 GB/s
PCIe 6.0	2022	64.0 GT/s	8.0 GB/s	128 GB/s
PCIe 7.0	2025	128.0 GT/s	16.0 GB/s	256 GB/s

Software S1 (separate file).

Modified CMAQ code: <https://github.com/kdo037/ROS3-CUDA>

CMAQ-CUDA simulation outputs: <https://zenodo.org/record/8274630>

SI References

1. D. W. Byun, Dynamically consistent formulations in meteorological and air quality models for multiscale atmospheric studies. Part II: Mass conservation issues. *Journal of the Atmospheric Sciences* **56**, 3808–3820 (1999).
2. EPA, CMAQv5.3 User Manual (2019) <https://doi.org/doi:10.5281/zenodo.3379043>.